

Thermodynamic phase stability, structural, mechanical, optoelectronic, and thermoelectric properties of the III-V semiconductor AlSb for energy conversion applications

Iskandar Raufov ^a, Dilshod Nematov ^{a,b,*} , Saidjafar Murodzoda ^a, Sakhidod Sattorzoda ^a, Anushervon Ashurov ^a

^a S.U. Umarov Physical-Technical Institute of NAST, Dushanbe 734063, Tajikistan

^b School of Optoelectronic Engineering & CQUPT-BUL Innovation Institute, Chongqing University of Posts and Telecommunications, Chongqing 400065, China

ARTICLE INFO

Keywords:

Aluminum antimonide (AlSb)
III-V semiconductors
Phase stability
Thermodynamic properties
Mechanical properties
Phonon dynamics
Electronic structure
Optoelectronic properties
Thermoelectric performance
Energy conversion materials
Infrared optoelectronics
Photovoltaic and thermoelectric applications

ABSTRACT

This study presents a first-principles investigation of the structural, thermodynamic, electronic, optical, and thermoelectric properties of aluminum antimonide (AlSb) in its cubic (F-43 m) and hexagonal (P6₃mc) phases. Both structures are dynamically and mechanically stable, which is confirmed by phonon calculations and the Born-Huang criteria. The lattice constants obtained using the SCAN and PBEsol functionals show good agreement with experimental data. The cubic phase has a direct band gap of 1.66–1.78 eV, while the hexagonal phase has 1.48–1.59 eV, as confirmed by mBJ and HSE06 calculations. Under external pressure, the band gap decreases in the cubic phase and increases in the hexagonal phase due to different s-p orbital hybridization mechanisms. The optical absorption coefficient reaches 10⁶ cm⁻¹, which is comparable to or higher than values known for other III-V semiconductors. The Seebeck coefficient exceeds 1500 $\mu\text{V/K}$ under intrinsic conditions, and the thermoelectric performance improves above 600 K due to enhanced phonon scattering and lattice anharmonicity. The calculated formation energies (-1.316 eV for F-43 m and -1.258 eV for P6₃mc) confirm that the cubic phase is thermodynamically more stable. The hexagonal phase shows higher anisotropy and lower lattice stiffness, which is beneficial for thermoelectric applications. These results demonstrate how crystal symmetry, phonon behavior, and charge transport are connected, and they provide useful guidance for the design of AlSb-based materials for optoelectronic and energy-conversion technologies.

1. Introduction

The development of modern technologies for energy conversion and information processing critically depends on the search for novel semiconducting materials with a comprehensive set of functional properties. In recent decades, halide perovskites, kesterites, CdTe, Si, GaAs, and related compounds have been extensively studied, achieving remarkable efficiencies in photovoltaic, thermoelectric, and optoelectronic devices [1–4]. However, despite their success, many of these materials face serious limitations, including poor thermal stability, moisture and UV degradation, phase instability, toxicity of certain components, and high production costs [5–7]. These limitations motivate the search for alternative semiconductors with improved reliability, technological compatibility, and large-scale applicability.

Aluminum antimonide (AlSb), a III-V semiconductor historically

known for its optoelectronic performance, has recently regained attention due to its unique combination of characteristics. It possesses a relatively wide band gap, high carrier mobility, and compatibility with III-V heteroepitaxy, making it attractive for infrared optoelectronics, photovoltaics, and thermoelectrics [8–10]. Phase engineering represents a particularly important aspect. While the cubic zinc-blende (F-43 m) phase is thermodynamically stable, the hexagonal wurtzite-like (P6₃mc) phase can be stabilized under epitaxial growth or nanoscale confinement, offering the potential for band gap tuning and modified functionalities [11–13]. Thermoelectric properties of bulk AlSb have traditionally been limited by relatively high lattice thermal conductivity and suboptimal conductivity/Seebeck balance, resulting in low ZT values [14]. Nevertheless, recent advances such as multiphonon scattering control, doping, composites, and nanostructuring provide pathways for improved performance [15–17]. Parallel studies on structurally

* Corresponding author.

E-mail address: dilnem@mail.ru (D. Nematov).

related Zintl phases (for example NaSrSb and NaBaSb) have reported ZT ≈ 2.0 at 900 K, attributed to ultralow lattice thermal conductivity and high Seebeck coefficients [18]. Similar design strategies have also been successfully applied to complex double perovskites (A_2AuScX_6), $\text{Ca}(\text{InP})_2$, and doped HgSe alloys, highlighting the broader relevance of structural-electronic tuning [19–23]. Recent studies have also reported significant progress in understanding the structural, optoelectronic, and thermoelectric behavior of AlSb and related III-V semiconductors. For example, pressure-driven band-gap engineering, defect-tolerant optical transitions, and mechanical tunability were demonstrated in several recent works [20–24]. These studies highlight the strong sensitivity of III-V compounds to bonding asymmetry, local coordination, and phase-dependent orbital hybridization, and emphasize the need for systematic comparative analyses of cubic and hexagonal polymorphs.

Recent studies of two-dimensional AlSb monolayers confirm a direct band gap of 0.93–1.65 eV, high carrier mobility, as well as strong excitonic effects and significant many-body interactions shaping the optical response [24]. For bulk crystals, pressure-induced structural transitions into denser NaCl -type (B1) and CsCl -type (B2) phases have been reported, accompanied by changes in electronic structure and mechanical properties [25–27]. Yet, systematic studies on phase competition between cubic (F-43 m) and hexagonal ($\text{P}6_3\text{mc}$) modifications remain scarce, with little data on relative total energies, phonon stability, thermodynamic properties, and complete sets of elastic constants [28].

In terms of practical opportunities, AlSb combines several advantages: technological compatibility with III-V devices, potential for infrared photodetectors and optoelectronics, tunable band structure via strain and doping, and radiation resistance, which is especially relevant for aerospace and defense applications [29]. In thermoelectrics, thermal transport processes play a decisive role. Recent works demonstrated that four-phonon scattering can strongly reduce the predicted thermal conductivity of III-V compounds (including AlSb), reshaping the understanding of intrinsic transport limits and offering new strategies for phonon engineering [15–17].

Despite this progress, several open questions remain, as comprehensive data are still lacking for the phonon stability of the hexagonal phase, its mechanical and thermoelectric characteristics, and the influence of defects and impurities on electronic and optical properties [28, 29]. Thermal transport processes, particularly multiphonon scattering, remain insufficiently explored, although they play a crucial role in determining the thermoelectric figure of merit [5, 30]. These gaps highlight the need for further investigations to uncover the hidden potential of AlSb as a multifunctional semiconductor of the next generation.

In this work, we perform a comprehensive first-principles study of the structural, mechanical, electronic, optical, thermodynamic, and thermoelectric properties of AlSb in both F-43 m and $\text{P}6_3\text{mc}$ phases, with emphasis on pressure-dependent stability and multifunctional potential.

2. Computational details

In this study, the structural, electronic, optical, mechanical, thermodynamic, and thermoelectric properties of aluminum antimonide (AlSb) in the cubic F-43 m and hexagonal $\text{P}6_3\text{mc}$ phases were investigated using density functional theory (DFT) as implemented in the VASP package [31]. The interactions between electrons and ions were described using the projector augmented-wave (PAW) method [32], with explicit consideration of the valence electron configurations: Al: $3s^23p^1$ and Sb: $4d^{10}5s^25p^3$. Structural optimization was performed using the SCAN functional [33] until the residual forces were below 0.01 eV/Å and the total energy convergence threshold was set to 10^{-6} eV. Convergence was achieved with a plane-wave cutoff energy of 700 eV and a Γ -centered k-point mesh of $7 \times 7 \times 7$ for the cubic F-43 m phase, and $12 \times 12 \times 12 \times 5$ for the hexagonal $\text{P}6_3\text{mc}$ phase of AlSb . To obtain a reliable estimation of the electronic band gap, both the

modified Becke-Johnson (mBJ) potential [34] and the hybrid HSE06 functional [35] were employed. The total and partial densities of states (DOS and PDOS), electronic band structures, and optical properties were calculated using the mBJ potential based on the SCAN-relaxed structures. Optical characteristics, including the dielectric function, absorption coefficient, and refractive index, were determined within the linear response formalism. Mechanical properties were evaluated using the GGA-PBE functional while preserving the SCAN-optimized geometry. The second-order elastic constants were obtained through the finite-strain method, and mechanical stability was assessed according to the Born-Huang criteria for cubic and hexagonal crystals. Phonon and thermodynamic properties were analyzed using the Phonopy package interfaced with VASP 6.4.3 via the finite-displacement method in a $2 \times 2 \times 2$ supercell. From the phonon density of states, Helmholtz free energy, entropy, and constant-volume heat capacity were calculated in the temperature range of 0–1000 K. The absence of imaginary frequencies in the phonon spectra confirmed the dynamical stability of all examined phases. Thermoelectric properties were evaluated using the BoltzTraP2 code interfaced with Quantum ESPRESSO 7.4.1 [36].

3. Results and discussion

3.1. Structural properties

Aluminum antimonide crystallizes in two structural modifications: a cubic phase with space group F-43 m and a hexagonal phase with space group $\text{P}6_3\text{mc}$. To ensure the reliability and accuracy of subsequent calculations, convergence tests were first performed to determine the optimal values of the plane-wave cutoff energy (ENCUT) and the k-point sampling density for Brillouin zone integration. Convergence with respect to both parameters was analyzed using the Monkhorst-Pack and Γ -centered schemes, allowing the selection of appropriate computational settings. As shown in Figure S1, once the cutoff energy reached 700 eV, the total energy of the system became stable for both phases under either sampling scheme. Further increases in ENCUT produced negligible changes in total energy while significantly increasing computational cost. This convergence approach is robust: despite minor variations in total energy behavior with respect to the k-point density, both sampling methods exhibit excellent convergence characteristics. This confirms the correctness of the chosen Brillouin zone discretization parameters and the reliability of the obtained computational results. In both phases, cubic and hexagonal, the Monkhorst-Pack and Γ -centered schemes yield nearly identical total energies, indicating the consistency and stability of the adopted electronic-structure modeling methodology.

Similarly, for both AlSb phases, k-point optimization was performed at $\text{ENCUT} = 315$ eV (approximately $1.3 \times \text{ENMAX}$), where the optimal meshes were determined to be $7 \times 7 \times 7$ (Γ -centered) for the cubic F-43 m phase and $12 \times 12 \times 5$ (Γ -centered) for the hexagonal $\text{P}6_3\text{mc}$ phase (Figure S2). These optimized ENCUT and k-point parameters were subsequently used as the standard computational setup for electronic-structure and optical-property calculations. Based on our observations, the Monkhorst-Pack grid ensures uniform Brillouin zone sampling without necessarily including the Γ point, which can be efficient for highly symmetric periodic systems. In contrast, the Γ -centered mesh explicitly includes the Γ point and often provides superior convergence for systems with lower symmetry or when accurate description of states near the Γ point is essential.

In the performed calculations, both discretization schemes exhibited excellent convergence of the total energy. The difference in total energy per atom between the two methods was < 1 meV, confirming that the chosen k-point density ensures sufficient numerical accuracy without unnecessary computational expense. After establishing the optimal computational parameters, full structural optimizations were carried out for both AlSb phases. The equilibrium lattice constants, unit cell volumes, and interaxial angles were determined and compared across different exchange-correlation functionals as well as with available

Table 1

Lattice parameters of cubic and hexagonal AlSb phases obtained with various exchange-correlation functionals.

AlSb	Lattice constants	PBE (GGA)	PBEsol	LDA	SCAN	Experimental
F43m	a (Å)	6.233	6.169	6.121	6.17	6.14 [37,38]
	$\alpha = \beta = \gamma$, °	90.00	90.00	90.00	90.00	
	V (Å ³)	242.15	234.77	229.33	235.11	
	c (Å)	4.39	4.34	4.31	4.35	
P6 ₃ mc	a (Å)	4.39	4.34	4.31	4.35	
	b (Å)	3.80	3.76	3.73	3.76	
	c (Å)	7.23	7.16	7.10	7.17	
	$\alpha = \beta \neq \gamma$, °	90, 12	90, 12	90, 12	90, 12	
	V (Å ³)	120.99	117.30	114.57	117.55	

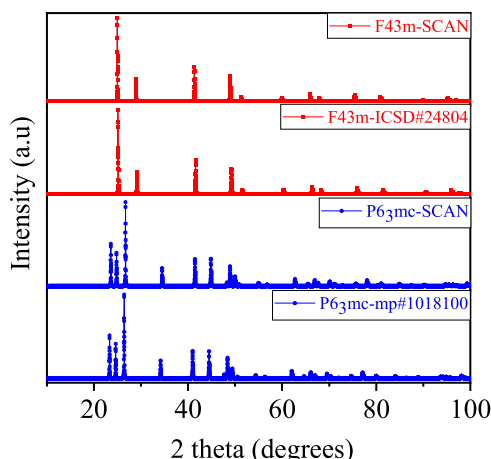


Fig. 1. Calculated X-ray diffraction (XRD) patterns for the cubic (F-43 m) and hexagonal (P6₃mc) phases of AlSb, obtained using Cu-K α radiation and visualized with the VESTA software.

experimental data (Table 1). The PBE functional belongs to the generalized gradient approximation (GGA) family, while PBEsol and SCAN are also GGA-based, with SCAN representing a more advanced meta-GGA formulation that improves accuracy for both structural and energetic predictions.

A comparative analysis of the lattice parameters reveals a consistent trend across both phases of AlSb: the PBE functional predicts the largest lattice constants, while LDA gives the smallest. The SCAN-derived lattice constant for the cubic phase ($a = 6.17$ Å) matches closely the experimental values of 6.14–6.15 Å, confirming the accuracy of the structural optimization [37,38]. The hexagonal phase also yields realistic lattice parameters that fall within the expected range predicted for wurtzite-like III–V structures, consistent with reported theoretical studies. The values obtained using PBEsol and SCAN lie between these two limits and are in closer agreement with experimental data. For example, for the cubic phase of AlSb, the calculated lattice constants are $a = 6.233$ Å (PBE), $a = 6.169$ Å (PBEsol), $a = 6.121$ Å (LDA), and $a = 6.172$ Å (SCAN). A similar trend is observed for the hexagonal phase. These differences arise from the intrinsic characteristics of the respective exchange-correlation functionals. PBE is known to slightly overestimate lattice volumes due to its weaker treatment of correlation effects. In contrast, LDA assumes a homogeneous electron gas approximation, which often results in underestimated lattice parameters. PBEsol, specifically designed for solid-state systems, provides more accurate equilibrium volumes, whereas SCAN, as a meta-GGA functional, offers improved reliability in predicting both structural and electronic properties.

Fig. 1 shows the calculated theoretical X-ray diffraction (XRD) patterns for both AlSb phases, simulated using Cu-K α radiation within the VESTA software package. The well-defined diffraction peaks confirm the

high crystallinity of both structures and are consistent with the expected symmetry characteristics of the cubic F-43 m and hexagonal P6₃mc phases.

The simulated diffraction profiles exhibit the characteristic peaks corresponding to the F-43 m and P6₃mc space groups, confirming the crystalline purity and the absence of secondary phases. The cubic phase, shown in red, was compared with the ICSD database, revealing a complete match of all major reflections without the appearance of additional peaks, which verifies the phase purity of the calculated cubic AlSb. The hexagonal phase, plotted in blue, was validated against the Materials Project database due to the absence of relevant ICSD data. The lack of extra peaks likewise confirms the structural purity of the hexagonal AlSb phase.

3.2. Phonon and thermodynamic properties

To assess the stability and thermal behavior of the AlSb phases, phonon, thermodynamic, and elastic properties were calculated. These parameters provide insights not only into the dynamical stability of the crystal lattice but also into its heat transport behavior and vibrational anharmonicity. Figures 2(a-d) present the phonon dispersion relations and phonon density of states (PhDOS) for the cubic and hexagonal phases of AlSb, calculated along the high-symmetry directions of the Brillouin zone. The absence of imaginary frequencies in both dispersion spectra (Figs. 2a,b) indicates that the optimized structures are dynamically stable, confirming the lack of soft modes that could lead to lattice instability. In the cubic phase, the optical phonon branches extend up to approximately 10 THz, suggesting stiffer interatomic bonding and a more rigid lattice. By contrast, the phonon spectrum of the hexagonal phase is shifted toward lower frequencies, reflecting softer lattice dynamics and higher vibrational anisotropy. In the phonon density of states, the low-frequency region (2–4 THz) is primarily dominated by vibrations of the heavier Sb atoms, while the high-frequency region (8–10 THz) corresponds to the lighter Al atoms (Figs. 2c,d). This mass-dependent separation of vibrational modes is typical for binary compounds with significant atomic mass contrast and plays a crucial role in defining their thermal transport characteristics.

Both AlSb phases are phonon-stable, yet the hexagonal structure exhibits lower stiffness, which can be advantageous for thermoelectric applications due to its potentially reduced lattice thermal conductivity. The sharper peaks observed in the Phonon DOS of the cubic phase imply a higher degree of atomic ordering and stronger covalent bonding, whereas the broader, smoother spectra of the hexagonal phase suggest enhanced lattice anharmonicity, which promotes phonon-phonon scattering and consequently lowers thermal conductivity.

Thus, both phases of AlSb exhibit no imaginary frequencies, confirming their dynamical stability in agreement with the thermodynamic results. The main phonon characteristics of both phases, including the range of acoustic modes and maximum vibrational frequencies, are summarized in Table 2.

The obtained data indicate that the cubic phase is characterized by higher phonon frequencies, reflecting stronger interatomic bonding and higher lattice thermal conductivity. In contrast, the hexagonal modification exhibits a softer lattice and pronounced vibrational anisotropy, which can reduce heat transport and enhance thermoelectric performance.

Subsequently, the temperature-dependent thermodynamic functions were analyzed in the range of 0–1000 K, including entropy S(T), Helmholtz free energy F(T), and constant-volume heat capacity Cv(T). These quantities were calculated from the phonon density of states g(ω) within the harmonic approximation, according to the following expressions:

$$F(T) = \int_0^{\infty} g(\omega) \left(\frac{1}{2} \hbar \omega + k_B T \ln(1 - e^{-\hbar \omega / k_B T}) \right) d\omega,$$

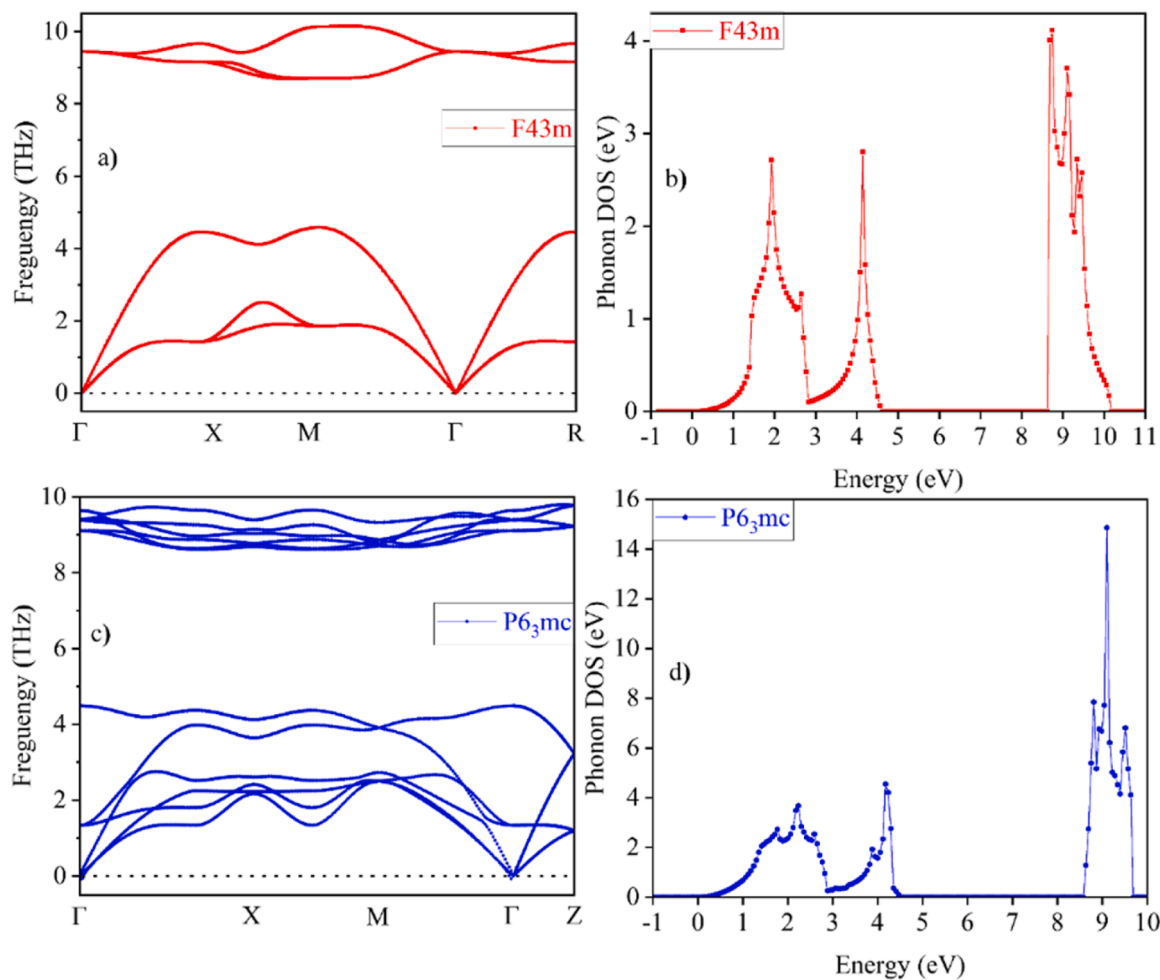


Fig. 2. Calculated (a) phonon dispersion curves and (b) phonon density of states (Phonon DOS) for the cubic (F-43 m) and hexagonal (P6₃mc) phases of AlSb.

Table 2
Phonon characteristics of the AlSb phases.

AlSb	Maximum Phonon Frequency (THz)	Acoustic Branch Range (THz)	Stability Indicator (Imaginary Frequencies)	Key Feature
F-43m	≈ 10	0–4	Absent	Rigid lattice with high structural stability
P6 ₃ mc	≈ 8.5	0–3.5	Absent	Soft lattice with pronounced anisotropy

$$S(T) = - \int_0^{\infty} g(\omega) [n(\omega, T) \ln n(\omega, T) - (1 + n(\omega, T)) \ln(1 + n(\omega, T))] d\omega,$$

$$C_V(T) = k_B \int_0^{\infty} g(\omega) \left(\frac{\hbar\omega}{k_B T} \right)^2 \frac{e^{\hbar\omega/k_B T}}{(e^{\hbar\omega/k_B T} - 1)^2} d\omega,$$

where $n(\omega, T) = \frac{1}{e^{\hbar\omega/k_B T} - 1}$ - is the Bose-Einstein distribution, \hbar is the reduced Planck constant, k_B -is the Boltzmann constant and ω represents the phonon frequency.

The calculations show that the thermodynamic behavior of both AlSb phases follows the classical anharmonic models and approaches the Dulong-Petit limit at high temperatures. This trend reflects the expected

Table 3
Comparison of thermodynamic characteristics of AlSb at 300, 600, and 900 K.

T, (K)	C _v (J·mol ⁻¹ ·K ⁻¹)	S (J·mol ⁻¹ ·K ⁻¹)	F (eV/ formula unit)	H (eV/ formula unit)	Remark
300	23–24	60–62	-18.92	-18.84	Phonon contribution indicates lattice stabilization
600	28–29	95–100	-18.70	-18.50	C _v approaches the Dulong-Petit limit
900	30–31	130–135	-18.45	-18.10	Anharmonicity increases; thermal stability maintained

saturation of the heat capacity and the stabilization of vibrational entropy with increasing temperature. The generalized numerical values of the thermodynamic parameters at selected characteristic temperatures are summarized in Table 3.

In Fig. 3a, which illustrates the temperature dependence of entropy, a monotonic increase in S(T) is observed for both phases, as expected. This behavior is attributed to the progressive activation of phonon modes with increasing temperature and the corresponding rise in lattice disorder.

The absolute entropy values show moderate differences between the two phases, which can be explained by variations in their structural rigidity and vibrational characteristics. The sensitivity of entropy to crystallochemical parameters thus makes it a valuable indicator for evaluating energy distribution and lattice stability under thermal

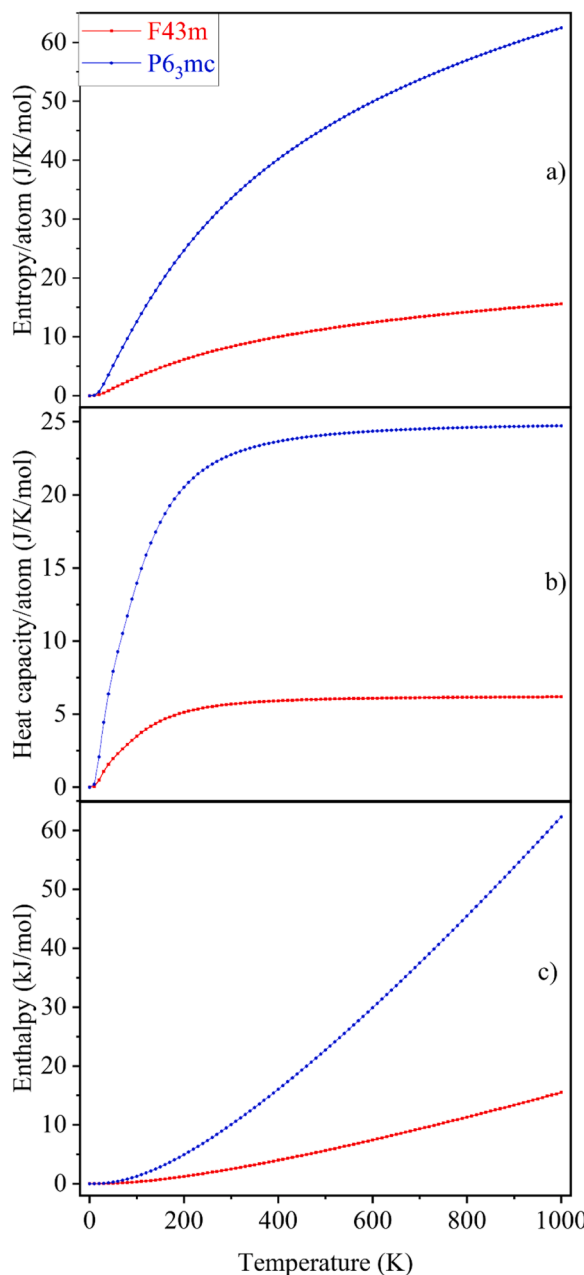


Fig. 3. Temperature dependence of (a) entropy, (b) heat capacity at constant volume, and (c) enthalpy for the cubic and hexagonal phases of AlSb.

excitation.

In Fig. 3b, the variation of constant-volume heat capacity with temperature shows that both phases exhibit the characteristic behavior predicted by quantum solid-state theory: a rapid increase in heat capacity at low temperatures followed by saturation at higher temperatures approaching the classical limit. The differences between the two curves reflect variations in the low-frequency phonon density of states, which predominantly governs heat capacity in the low-temperature region. This comparison highlights how the structural features of the crystal lattice directly influence the material's ability to store thermal energy, a topic further discussed in the section on the thermoelectric properties of AlSb. Fig. 3c illustrates the temperature dependence of enthalpy, which increases steadily with temperature. This growth indicates that, upon heating, the system absorbs a certain amount of thermal energy, leading to an increase in the internal energy of atoms and phonons. As the temperature rises, atomic vibrations intensify,

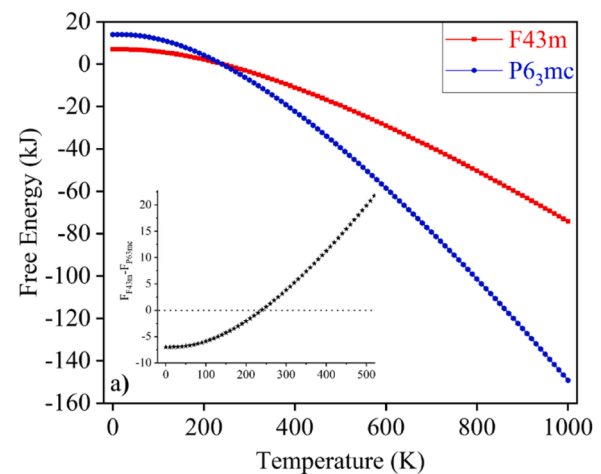


Fig. 4. Temperature dependence of the Helmholtz free energy of AlSb.

producing a pronounced increase in enthalpy. The continuous rise of $H(T)$ with temperature confirms that AlSb remains thermodynamically stable throughout the investigated range.

Fig. 4 presents the Helmholtz free energy $F(T)$ as a function of temperature, representing the total thermodynamic potential of the system. The observed decrease in $F(T)$ with increasing temperature for both phases results from the growing entropic contribution and aligns with the general thermodynamic behavior expected for condensed matter systems.

Although the differences between the two phases are relatively small, they persist and become more pronounced at higher temperatures, indicating distinct degrees of thermodynamic stability. As shown in Fig. 4, AlSb exhibits a phase transition near 245–250 K. Lower values of the Helmholtz free energy correspond to a more stable configuration at a given temperature, which is particularly important when evaluating materials for high-temperature applications. The analysis confirms the overall stability of both phases across a wide temperature range. Additionally, the calculated formation energies are **-1.316 eV** for the F-43 m and **-1.258 eV** for the P6₃mc phase, confirming the higher thermodynamic stability of the cubic modification. Direct comparison with literature values is difficult because reliable experimental formation energies for AlSb are not available, and existing theoretical reports for the cubic phase vary considerably depending on the exchange-correlation functional and reference potentials. These results are consistent with the phonon and thermodynamic analyses and establish a foundation for future thermodynamic modeling, including phase diagram construction and assessment of stability during the formation of solid phases and heterostructures. For a more detailed understanding of the thermodynamic and phonon-related stability, Figs. 9a-b present the calculated pressure-dependent elastic moduli (C_{11} , C_{12} , C_{44} , etc.) within the 0–30 GPa range for both phases. The complete set of elastic constants is provided in Table S2.

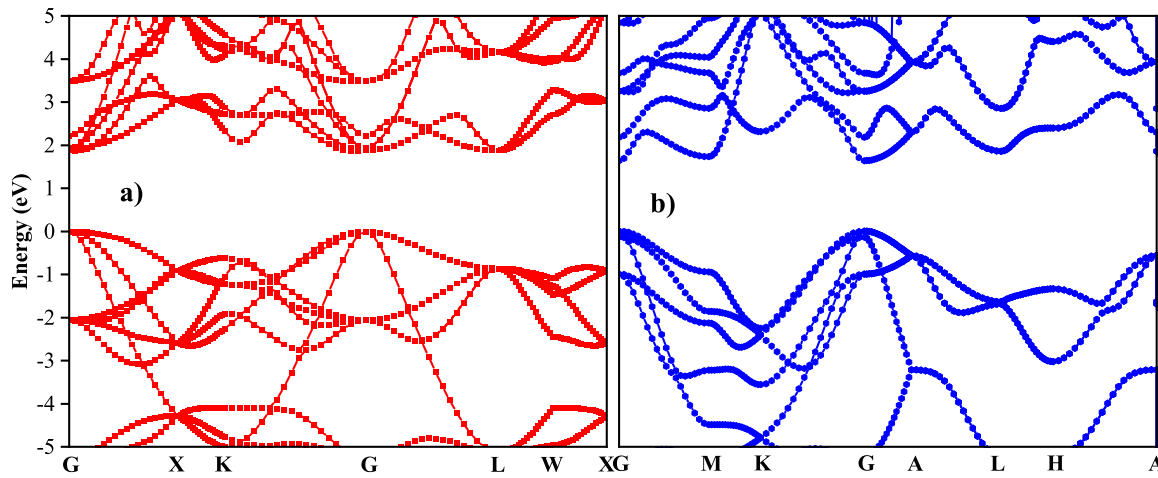
3.3. Electronic structure of alsb

After comprehensive structural optimization, the electronic band structures of both AlSb phases were computed and analyzed to evaluate key electronic parameters such as band gap, band dispersion, and total and partial density of states. Based on the well-optimized geometries obtained using GGA, PBEsol, LDA, and SCAN functionals, the band gaps were further refined employing the hybrid HSE06 functional and the modified Becke-Johnson (mBJ) potential. The comparative results are presented in Table 4.

The obtained results show that, regardless of the exchange-correlation functional used, both the hybrid HSE06 and the modified Becke-Johnson (mBJ) potential yield band gap values that are in close

Table 4Comparison of the calculated band gap (E_g) values for the cubic and hexagonal phases of AlSb using the HSE06 and mBJ methods.

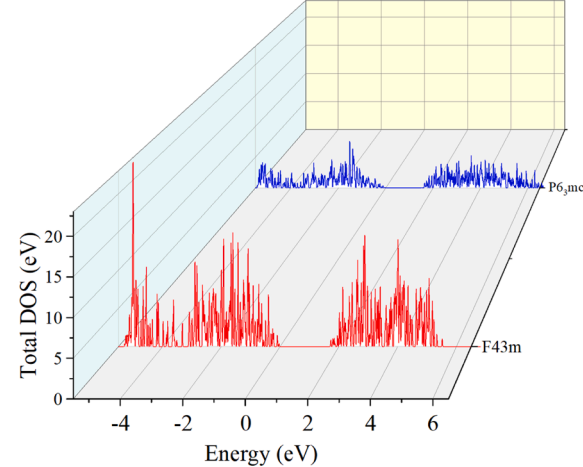
AlSb	HSE06/LDA	HSE06/PBE	HSE06/PBEsol	HSE06/SCAN	mBJ/LDA	mBJ/PBE	mBJ/PBEsol	mBJ/SCAN	EXPERIMENTAL
F43m	1.715	1.781	1.737	1.748	1.661	1.716	1.672	1.683	1.63 ^[39] , 1.75 ^[40] , 1.81 ^[41]
P6 ₃ mc	1.595	1.496	1.584	1.584	1.529	1.408	1.485	1.485	-

**Fig. 5.** Calculated electronic band structures of cubic (a) and hexagonal (b) phases of AlSb.

agreement with each other and consistent with experimental observations. Spin-orbit coupling (SOC) was not included because previous studies showed that SOC induces only a small shift in the band edges of AlSb due to the relatively light mass of Al and moderate SOC strength of Sb. Therefore, the direct bandgap character and optical transitions remain unchanged, and the mBJ/HSE06 results remain reliable [42]. For the cubic F-43 m phase, the calculated band gap varies between 1.66 and 1.78 eV, which agrees well with the experimental range of 1.63–1.81 eV [39–41]. This consistency confirms the reliability of the selected computational methods and the accuracy of the treatment of exchange-correlation effects in the AlSb system.

In contrast, the hexagonal P6₃mc modification exhibits a slightly narrower band gap, indicating stronger overlap between the valence and conduction bands and potentially higher carrier mobility. The reduction of E_g compared with the cubic phase arises from changes in local coordination and reduced lattice symmetry, which result in denser packing of electronic states and weaker hybridization between the Al and Sb s and p orbitals. Comparison across different functionals shows that LDA and PBE systematically underestimate E_g due to self-interaction errors, while SCAN and particularly HSE06 provide more realistic results. The mBJ potential demonstrates comparable accuracy to HSE06, differing by only 0.05–0.07 eV, but with significantly lower computational cost. These findings confirm that both HSE06 and mBJ are reliable tools for accurately describing the electronic band structure of AlSb and analyzing how crystallochemical factors affect the band gap in both phases. The strong agreement between HSE06 and mBJ has been repeatedly validated in previous studies [42–59].

The band structure diagrams presented in Fig. 5, plotted along the high-symmetry directions of the Brillouin zone, reveal that both AlSb phases possess a direct band gap transition from the valence to the conduction band, which is a crucial property for modern optoelectronic devices. The analysis shows that both phases behave as semiconductors with a well-defined separation between valence and conduction states. The cubic phase exhibits a slightly wider band gap, whereas the hexagonal phase has a narrower one, consistent with the results in Table 4. Both structures feature an extended electronic dispersion, an important factor for improving the performance of photovoltaic materials since the main part of the solar spectrum falls within this energetic region.

**Fig. 6.** Calculated total electronic density of states (DOS) of AlSb using the HSE06 functional.

The presence of a direct band gap promotes efficient generation and recombination of electron-hole pairs in the studied material. This property enhances both light absorption and photoluminescence, which are critical for the performance of optoelectronic devices such as light-emitting diodes (LEDs) and lasers. Moreover, materials with a wide and direct band gap can reduce energy losses caused by thermal conductivity and enable stable operation of electronic components under high voltage, an important aspect in the design of photovoltaic modules.

Furthermore, the calculated density of states (DOS) complements the band structure diagrams shown in Fig. 5 and confirms the observed electronic trends. The DOS analysis provides additional insight into the evolution of electronic properties, offering a consistent description of the orbital contributions and hybridization effects in both phases (Fig. 6).

As shown in Fig. 6, the transition from the cubic to the hexagonal phase leads to a narrowing of the band gap. The primary distinction between the two phases lies in the changes in their electronic structure

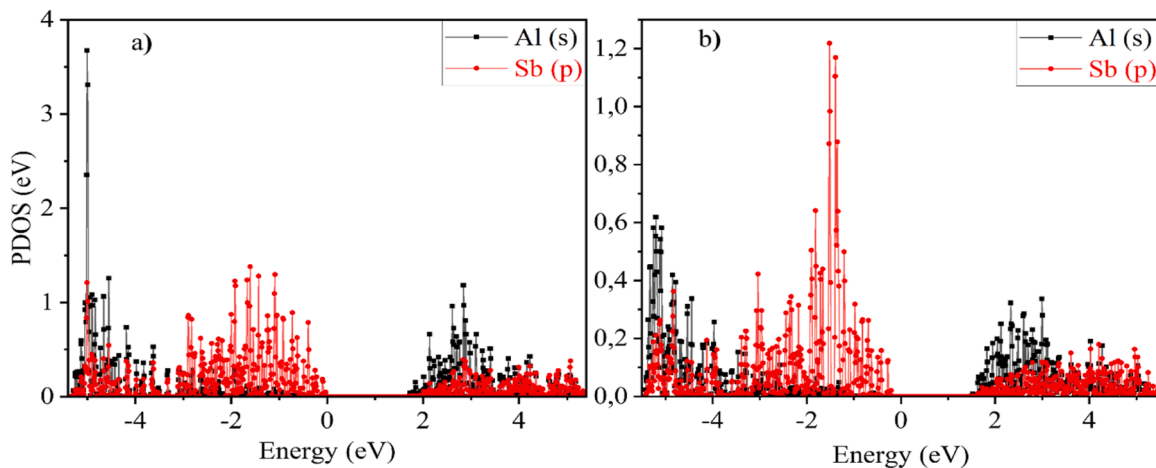


Fig. 7. Partial electronic density of states (PDOS) for the cubic (a) and hexagonal (b) phases of AlSb.

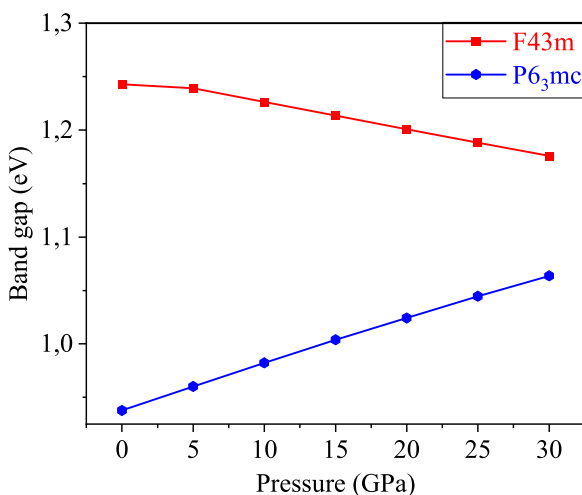


Fig. 8. Dependence of the band gap width of the cubic (red) and hexagonal (blue) phases of AlSb on external pressure, calculated in the range of 0–30 GPa.

near the band edges. At the same time, variations in the density of states close to the Fermi level affect both electrical conductivity and the generation of charge carriers. These effects are important for tuning the material's properties for solar energy conversion and microelectronic

applications.

To gain a deeper understanding of the contributions of individual atoms to the formation of the valence and conduction bands, the partial density of states (PDOS) was analyzed, as shown in Figs. 7a,b. The PDOS results reveal a clear contribution from the Sb p-orbitals and Al s-orbitals to the overall electronic structure. In both phases, the valence band is primarily composed of Sb p-orbitals, while the conduction band is mainly derived from Al s-orbitals.

In the cubic phase, a pronounced peak appears in the range from -4 to -5 eV, originating from the Al s-orbitals. This feature is absent in the hexagonal phase. The main contribution to the electronic density near the Fermi level comes from the Sb p-orbitals, which play a dominant role in defining the valence band. The PDOS spectra are in good agreement with the previously calculated band structures shown in Fig. 5.

3.3.1. Pressure-Dependent band gap evolution

In addition to the structural, phonon, thermodynamic, and electronic analyses, the variation of the electronic structure under external pressure was investigated to evaluate the evolution of the band gap and the mechanical and acoustic properties of AlSb. This approach provides insight into the stability of the material under mechanical stress. The calculated band gap values obtained using the GGA-PBE functional are summarized in Table S1 and reveal a clear and consistent trend. As shown in Fig. 8, in the cubic phase the band gap decreases with increasing external pressure within the 0–30 GPa range, while in the hexagonal phase it increases linearly with pressure. This opposite

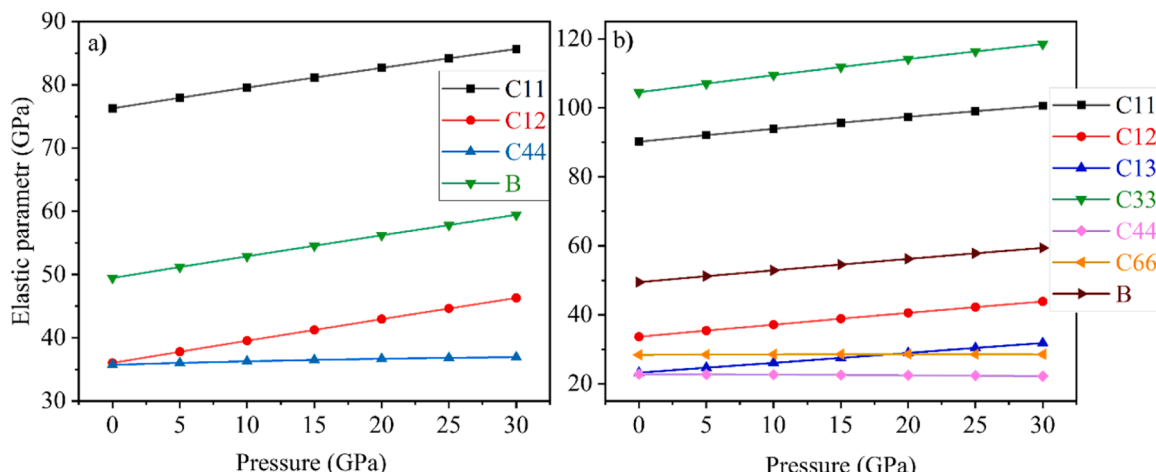


Fig. 9. Pressure dependence of the elastic constants C_{ij} (GPa) and bulk modulus B for AlSb: (a) cubic phase and (b) hexagonal phase.

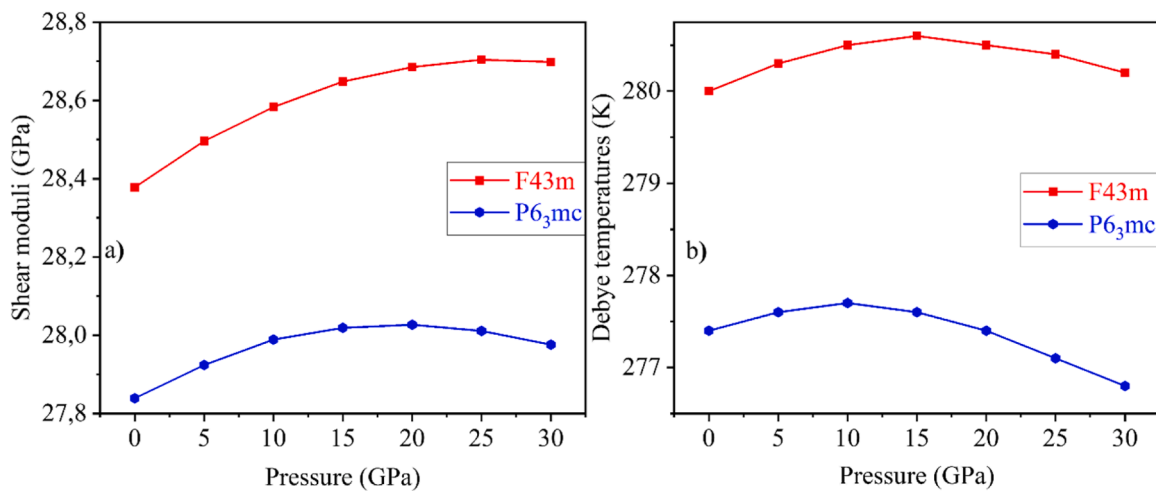


Fig. 10. Pressure dependence of (a) shear modulus (G) and (b) Debye temperature (Θ_D) for AlSb.

behavior arises from differences in the deformation response of the crystal lattices and the nature of the orbital hybridization between Al and Sb atoms.

In the cubic structure, compression enhances the overlap between Sb p-orbitals and Al s-orbitals, which lowers the conduction band minimum and reduces E_g . In contrast, in the hexagonal P6₃mc modification, changes in interatomic distances lead to a weakening of orbital overlap near the Γ point and to an increase in the energy separation between the valence and conduction bands. Overall, the opposite pressure-dependent trends of E_g reflect the different bonding characteristics and electronic-state symmetries of the two AlSb phases.

3.4. Mechanical properties and pressure effects

To understand how the pressure-induced evolution of electronic properties correlates with macroscopic stability, the mechanical characteristics of AlSb were calculated. Figs. 9a and 9b show the pressure-dependent elastic constants (C_{11} , C_{12} , C_{44} , etc.) and bulk modulus (B) for both phases in the range of 0–30 GPa. The complete set of elastic coefficients is listed in Table S2. The results indicate that both phases exhibit positive elastic constants (C_{ij}), satisfying the Born stability criteria for crystalline materials. This confirms that the AlSb system remains mechanically stable under the investigated pressure range, with no indication of shear instability or lattice softening. The increase in

elastic moduli with pressure also suggests enhanced lattice stiffness and reduced compressibility, which is consistent with the observed pressure dependence of the band gap and phonon spectra.

As shown in Fig. 9, both phases demonstrate a consistent increase in the main elastic parameters with rising pressure. This effect is particularly evident for the longitudinal stiffness components C_{11} and C_{33} , which reflect the growing rigidity of the lattice under compression. In contrast, the shear components C_{44} and C_{66} (for the hexagonal phase) remain nearly constant or slightly decrease, which can be attributed to the redistribution of internal stresses within the crystal structure.

Calculations were also carried out for the shear modulus (G), Debye temperature (Θ_D), and acoustic velocities, including the transverse (V_t), longitudinal (V_l), and average sound velocities (V_m). The corresponding results are presented in Figs. 10a,b and 11a,b, and the complete numerical data are summarized in Table S3. These parameters are directly linked to the phonon properties and describe the stiffness of the lattice as well as its ability to sustain thermal vibrations. The increase in Θ_D and V_m with pressure reflects stronger interatomic bonding and reduced anharmonic effects, in full agreement with the trends observed in the phonon spectra.

According to the results, both phases exhibit a similar trend: the values of G and Θ_D increase with pressure up to approximately 15 GPa and then gradually decrease. Throughout the entire pressure range, the cubic phase maintains higher values of these parameters, which

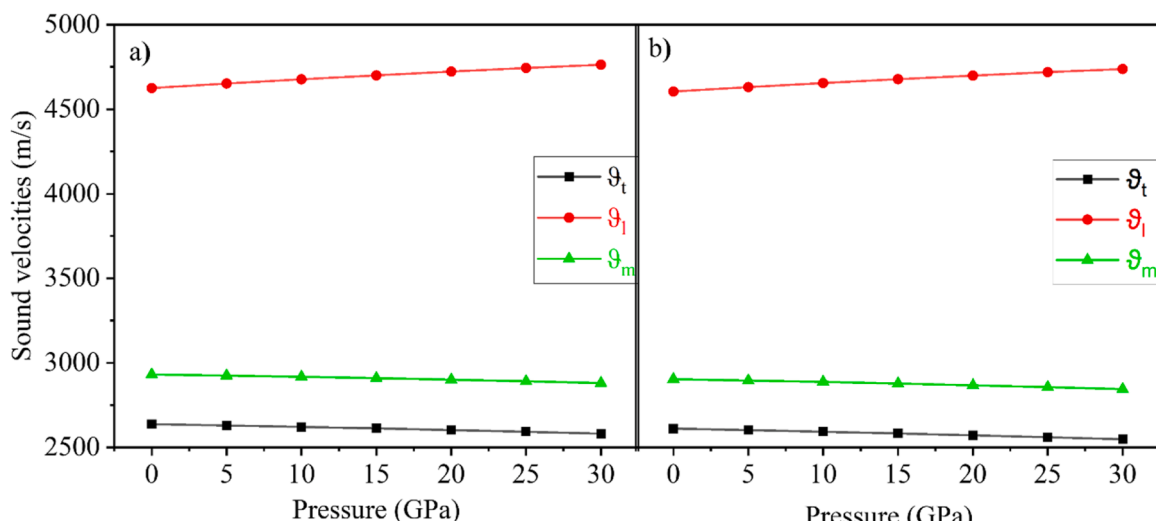


Fig. 11. Pressure dependence of longitudinal, transverse, and average sound velocities for (a) the cubic and (b) the hexagonal phases of AlSb.

Table 5

Pressure-dependent mechanical parameters of the cubic and hexagonal phases of AlSb obtained from GGA-PBE calculations.

Mechanical properties AlSb	P (GPa)	B (GPa)	E (GPa)	ν	M (GPa)	B/G
F43m	0	49.457	71.466	0.259	87.295	1.743
	5	51.188	72.106	0.265	89.182	1.796
	10	52.893	72.661	0.271	91.004	1.850
	15	54.550	73.139	0.277	92.747	1.904
	20	56.206	73.544	0.282	94.453	1.959
	25	57.832	73.887	0.287	96.104	2.015
	30	59.433	74.157	0.292	97.697	2.071
P6 ₃ mc	0	49.452	70.321	0.263	86.571	1.776
	5	51.191	70.883	0.269	88.423	1.833
	10	52.867	71.371	0.275	90.185	1.889
	15	54.556	71.770	0.281	91.914	1.947
	20	56.197	72.095	0.286	93.566	2.005
	25	57.822	72.350	0.291	95.170	2.064
	30	59.396	72.539	0.296	96.698	2.123

confirms its greater mechanical rigidity and thermal stability compared to the hexagonal modification. The observed behavior reflects the strengthening of interatomic interactions at moderate compression and their partial relaxation under higher external pressure, consistent with the general tendencies of covalent semiconductors.

The analysis of sound velocity as a function of pressure (Fig. 11, Table S3) provides deeper insight into the dynamic stability and acoustic stiffness of AlSb. Both phases show a clear tendency for V_t and V_m to decrease with increasing pressure from 0 to 30 GPa. This behavior is typical for dense crystalline materials where compression weakens shear-related phonon modes. In the cubic phase, the average sound velocity V_m decreases from 2930 m/s to 2880 m/s, while the transverse velocity V_t slightly drops from 2638 m/s to 2637 m/s, indicating a limited ability of the material to efficiently transmit shear vibrations.

In contrast, the longitudinal velocity V_l shows a consistent increase, rising from 4625 m/s at 0 GPa to 4763 m/s at 30 GPa (Fig. 11a, Table S3). This trend can be attributed to enhanced bulk stiffness and the preservation of high density along longitudinal directions. The simultaneous decrease in V_t and V_m suggests a degree of anisotropy in the acoustic response under pressure. The cubic phase exhibits higher absolute values of all three velocity components compared with the hexagonal phase. At 0 GPa, V_l reaches 4625 m/s, while V_t and V_m are 2637 m/s and 2931 m/s, respectively. Even at 30 GPa, these values remain relatively high (4763 m/s, 2582 m/s, and 2881 m/s), confirming the strong acoustic stiffness of the cubic modification and its potentially higher thermal conductivity. This feature is particularly advantageous

for optoelectronic and thermoelectric applications, where efficient heat management is crucial for device reliability.

Based on the GGA-PBE calculations, additional mechanical properties, including the bulk modulus (B), Young's modulus (E), Poisson's ratio (ν), longitudinal modulus (M), and Pugh's ratio (B/G), were evaluated and are summarized in Table 5. The results reveal that the cubic phase exhibits greater overall stiffness. A gradual increase in E, G, and B is observed with pressure, reflecting enhanced interatomic bonding and resistance to deformation. The B/G ratio exceeds 1.75 for both phases, which indicates ductile mechanical behavior and anisotropic bonding characteristics. The maximum value of B/G (2.123) is obtained for the hexagonal phase at 30 GPa, suggesting a partial softening of the lattice and an increase in plasticity under compression.

As shown in Table 5 and Figs. 2-4, the cubic phase exhibits higher values of the main mechanical and thermodynamic parameters across the entire pressure range. At 0 GPa, its bulk modulus reaches 49.5 GPa, and the Young's modulus is 71.5 GPa, both of which are greater than those of the hexagonal phase. With an increase in pressure to 30 GPa, the bulk modulus of the cubic phase rises to 59.4 GPa, indicating strong resistance to volumetric compression. Similarly, its shear modulus under ambient conditions is 28.4 GPa, and the transverse sound velocity equals 2637 m/s, both higher than those observed for the hexagonal structure.

The Debye temperature (Θ_D) for the cubic phase reaches 280 K, compared to 277.4 K for the hexagonal phase. This difference reflects a stiffer phonon lattice and potentially higher thermal conductivity of the cubic structure. With increasing pressure up to 15 GPa, both the shear modulus (G) and Debye temperature (Θ_D) gradually increase, followed by a slight decrease at higher pressures. Nevertheless, even at 30 GPa, the cubic phase maintains superior values of these parameters, confirming its high mechanical and thermal robustness. Fig. 12 presents the pressure dependence of the lattice parameters (a, b, c) and unit cell volume for both AlSb phases. As the pressure increases, all lattice parameters decrease nearly linearly, consistent with the compressibility behavior typical of crystalline solids. In the cubic phase, compression leads to a more pronounced reduction in volume compared with the hexagonal phase, indicating higher compressibility of the cubic structure. In contrast, the hexagonal modification exhibits nearly uniform contraction along the a, b, and c axes, reflecting moderate anisotropy and stability against structural distortions under compression.

Overall, both AlSb phases demonstrate elastic stability within the investigated pressure range of 0–30 GPa. However, the hexagonal structure shows slightly lower deformation rates and potentially greater mechanical reliability under sustained pressure, while the cubic phase remains the stiffer and thermally more conductive polymorph.

The results shown in Fig. 12 illustrate stable and physically

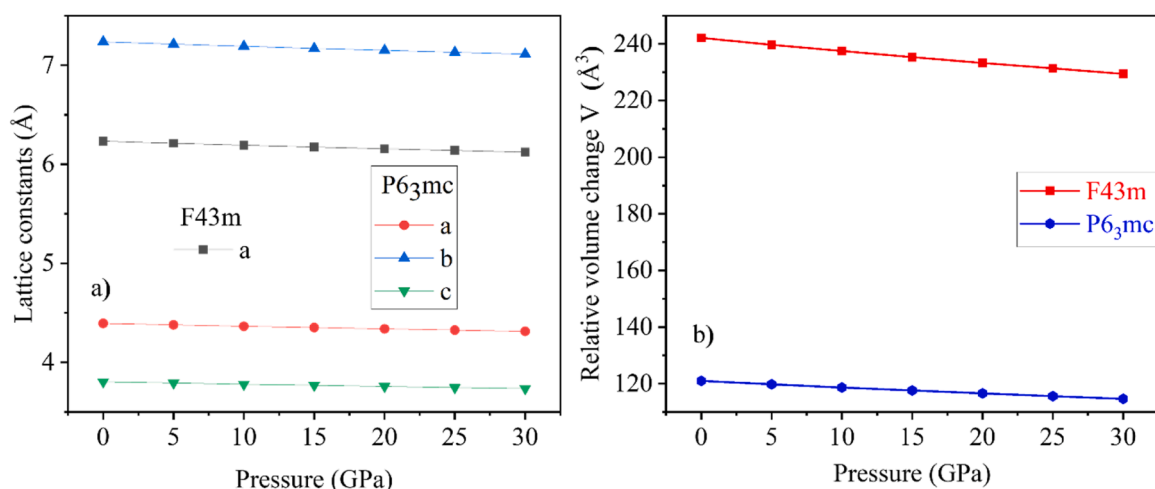


Fig. 12. Pressure dependence of the lattice parameters and relative unit cell volume of AlSb: (a) lattice constants, (b) relative volume variation.

consistent behavior of both AlSb phases under external pressure. The in-plane and out-of-plane lattice parameters, as well as the unit cell volume, decrease systematically with increasing pressure from 0 to 30 GPa. This trend reflects the elastic compressibility of the crystal lattice and confirms the absence of any pressure-induced phase transitions within the investigated range.

3.5. Optical properties

To further evaluate the optical response of AlSb, the real (ϵ_1) and imaginary (ϵ_2) parts of the dielectric function were calculated for both the cubic F-43 m and hexagonal P6₃mc phases (Figures S3 and S4). Optical phenomena including absorption coefficient ($\alpha(\omega)$), energy loss function ($L(\omega)$), extinction coefficient ($k(\omega)$), reflectivity ($R(\omega)$), and refractive index ($n(\omega)$) are present in all types of materials and can be studied at both microscopic and macroscopic levels. In bulk materials, the complex permittivity is closely related to the band structure at the microscopic or quantum mechanical level [60–62]. Optical properties such as the refractive index and absorption coefficient indicate the response of the material when photons hit them. The real part of the permittivity, which is considered an inherent property of any material, indicates the stored energy that can be released at zero energy or frequency limit. Using the Ab initio calculation algorithms implemented in the VASP code, the complex imaginary permittivity can be obtained in the PAW method by summation over conduction bands, where the expression obtained in [63] for determining $\epsilon_2(\omega)$ has the following form:

$$\epsilon_2^{\alpha\beta}(\omega) = \frac{4\pi^2 e^2}{\Omega} \frac{1}{q^2} \lim_{q \rightarrow 0} \sum_{c,\vartheta,k} 2\omega_k \delta(\epsilon_{ck} - \epsilon_{\vartheta k} - \omega) \times \langle u_{ck+e_\alpha q} | u_{ck} \rangle \langle u_{ck+e_\alpha q} | u_{\vartheta k} \rangle^* \quad (1)$$

In the above equation the transitions are made from occupied to unoccupied states within the first Brillouin zone, the wave vectors are fixed k . Real (ϵ_1) and Imaginary (ϵ_2) parts of analytical dielectric function are connected by the Kramers - Kronig relations [64],

$$\epsilon_1^{\alpha\beta}(\omega) = 1 + \frac{2}{\pi} P \int_0^\infty \lim_{q \rightarrow 0} \frac{\epsilon_2^{\alpha\beta}(\omega') \omega'}{\omega'^2 - \omega^2 + i\eta} d\omega' \quad (2)$$

Given Eq. (1–2), the optical conductivity spectrum (σ), energy loss spectrum (L), refractive index (n), reflection coefficient (R), absorption coefficient (α), and extinction coefficient (k) may be calculated as follows:

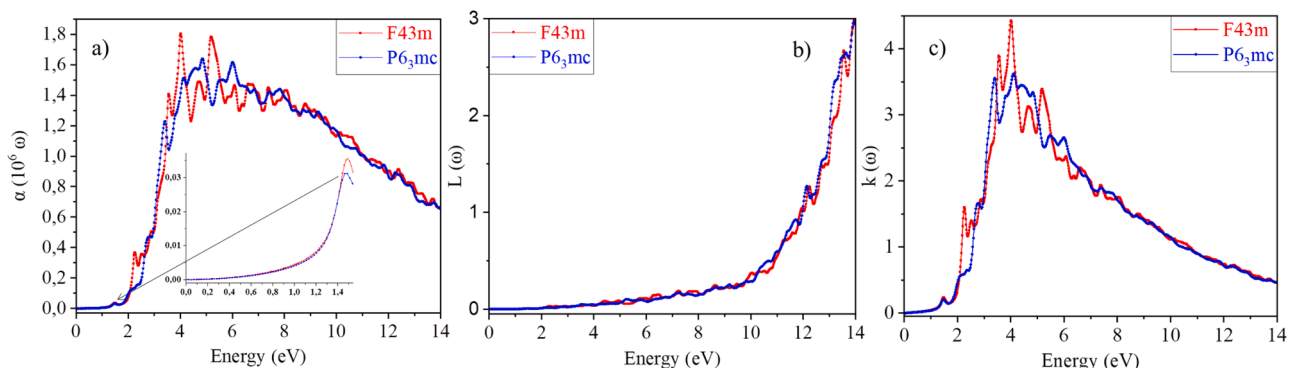


Fig. 13. Calculated spectra of (a) absorption coefficient $\alpha(\omega)$, (b) energy loss function $L(\omega)$, and (c) extinction coefficient $k(\omega)$ for cubic (red) and hexagonal (blue) phases of AlSb.

$$R(\omega) = \left| \frac{\sqrt{\epsilon(\omega)} - 1}{\sqrt{\epsilon(\omega)} + 1} \right|^2 \quad (3)$$

where $\epsilon(\omega) = \epsilon_1(\omega) + i\epsilon_2(\omega)$.

$$L(\omega) = \frac{\epsilon_2(\omega)}{\epsilon_1^2(\omega) + \epsilon_2^2(\omega)} \quad (4)$$

$$n(\omega) = \left| \frac{\sqrt{\epsilon_1^2 + \epsilon_2^2} + \epsilon_1}{2} \right|^{\frac{1}{2}} \quad (5)$$

$$k(\omega) = \left| \frac{\sqrt{\epsilon_1^2 + \epsilon_2^2} - \epsilon_1}{2} \right|^{\frac{1}{2}} \quad (6)$$

$$\alpha(\omega) = \frac{2\omega k(\omega)}{c} = \frac{\epsilon_2(\omega)\omega}{n(\omega)c} \quad (7)$$

$$\sigma(\omega) = \sigma_1(\omega) + i\sigma_2(\omega) = -i \frac{\omega}{4\pi} [\epsilon(\omega) - 1] = \frac{\epsilon_2(\omega)\omega}{4\pi} + i \frac{1 - \epsilon_1(\omega)\omega}{4\pi} \quad (8)$$

From these quantities, key optical parameters were derived, including the absorption coefficient ($\alpha(\omega)$), energy loss function ($L(\omega)$), extinction coefficient ($k(\omega)$), reflectivity ($R(\omega)$), and refractive index ($n(\omega)$). Fig. 13 (a–c) presents the computed spectra of the absorption coefficient $\alpha(\omega)$, the energy loss function $L(\omega)$, and the extinction coefficient $k(\omega)$ for both AlSb phases. The results show typical semiconductor

like behavior, where the absorption onset occurs in the range of 1.6–1.7 eV, consistent with the calculated band gap. In the low-energy region, the sharp rise in $\alpha(\omega)$ indicates direct interband transitions, while multiple pronounced peaks appear between 4–8 eV, corresponding to electronic transitions from the Sb p-states in the valence band to the Al s/p-states in the conduction band. The maximum absorption coefficient 10^6 cm^{-1} is comparable to or higher than that of GaSb, InSb, and AlP thin films reported in recent works [65–72], indicating that AlSb can efficiently absorb UV-visible photons.

The stronger maxima observed for the hexagonal phase indicate a higher density of accessible states near the Fermi level, which enhances the probability of optical transitions and accounts for its stronger high-energy response. The energy loss function (Fig. 13b) shows a dominant plasmon peak near 13 eV for both phases, corresponding to collective

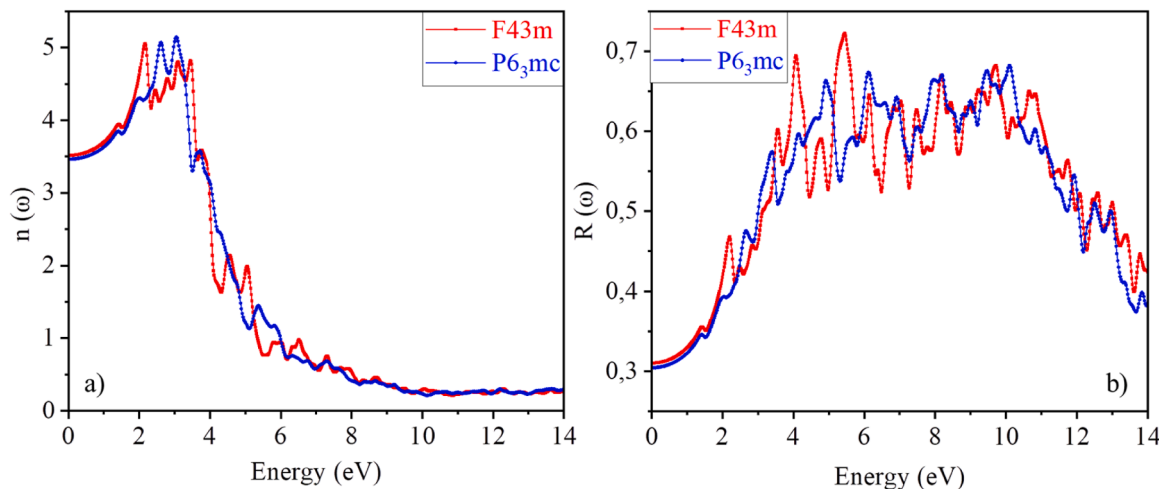


Fig. 14. Calculated spectra of (a) refractive index $n(\omega)$ and (b) reflectivity $R(\omega)$ for cubic (red) and hexagonal (blue) phases of AlSb.

Table 6

Static optical parameters of cubic and hexagonal phases of AlSb, including the refractive index $n(0)$, real part of the dielectric constant $\epsilon_1(0)$, and reflectivity $R(0)$.

AlSb	$\epsilon_1(0)$	$n(0)$	$R(0)$
F43m	12.344	3.51	0.310
P6 ₃ mc	11.994	3.46	0.305

oscillations of the electron gas and revealing similar plasma energies for the two structures. The extinction coefficient (Fig. 13c) follows the general trend of the absorption spectrum, peaking in the 4–6 eV range and gradually decreasing at higher photon energies, reflecting the dispersive nature of the optical response. The absorption coefficients of both phases reach magnitudes on the order of 10^6 cm^{-1} , which is typical for highly efficient light-harvesting materials and makes AlSb a strong candidate for thin-film photovoltaic applications. In the photon energy range of 2–12 eV, both phases display multiple resonance peaks associated with interband transitions. Overall, the AlSb phases exhibit high transparency in the visible region and strong absorption in the ultraviolet range, making them promising for photonics and optoelectronic device applications such as photodetectors, LEDs, and solar absorbers. It should be noted that the present optical calculations do not explicitly include excitonic effects, optical anisotropy, or local-field effects. These factors may slightly modify the absorption edge, especially in the

ultraviolet region. However, previous studies on III–V semiconductors show that such effects mainly lead to minor spectral shifts and do not change the general absorption trends.

Fig. 14 shows the spectra of the refractive index $n(\omega)$ and reflectivity $R(\omega)$ for the F-43 m and P6₃mc phases of AlSb, with their static values summarized in Table 6. In the low-energy region, both modifications display the typical semiconductor behavior characterized by a sharp rise in $n(\omega)$ as the photon energy approaches the optical absorption threshold. The maximum refractive index for the cubic phase reaches approximately $n_{\max} \approx 5.2$ at about 2.1 eV, while for the hexagonal phase, it is slightly higher ($n_{\max} \approx 5.4$ at 2.0 eV).

These values are comparable to those reported for other III–V semiconductors such as InSb and GaSb, reflecting the high polarizability and strong covalent bonding nature of the Al–Sb system. The high refractive index suggests strong light-matter interaction, which is beneficial for enhancing optical confinement in nanoscale devices. Additionally, the reflectivity spectra exhibit moderate values (up to 60 %), indicating efficient coupling of incident light into the material without excessive surface reflection, a desirable feature for photovoltaic and optoelectronic applications where both absorption and internal photon management are crucial.

The reflectivity coefficient $R(\omega)$ (Fig. 14b) exhibits a similar energy-dependent trend, with a maximum of $R_{\max} \approx 0.73$ for the cubic F-43 m phase and ≈ 0.75 for the hexagonal P6₃mc phase in the 2–3 eV range, followed by a gradual decline with increasing photon energy. The high

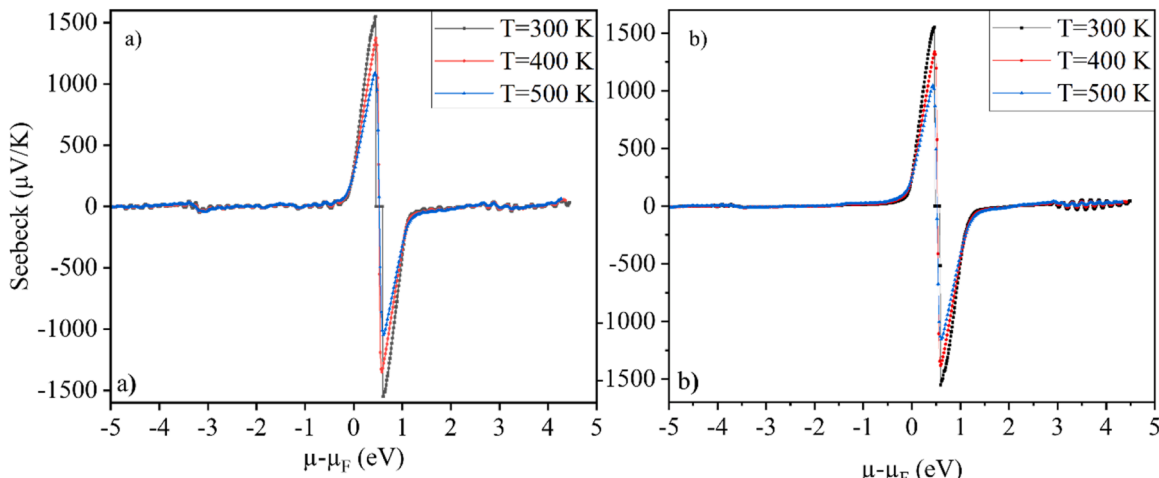


Fig. 15. Seebeck coefficient for (a) the cubic and (b) the hexagonal phases of AlSb at 300 K, 400 K, and 500 K.

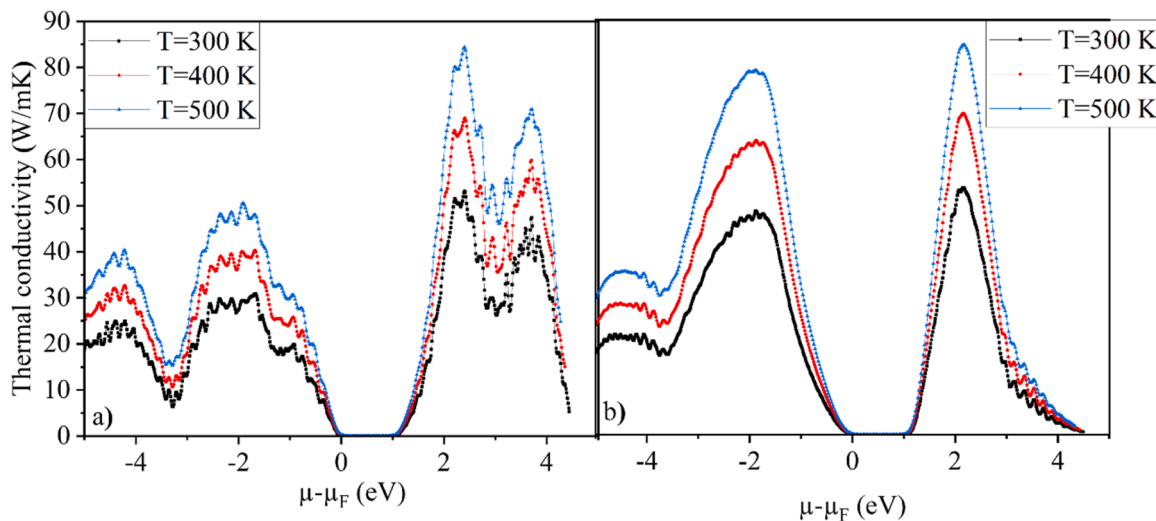


Fig. 16. Thermal conductivity of (a) cubic and (b) hexagonal AlSb phases at 300 K, 400 K, and 500 K.

reflectivity values observed in the visible and near-UV regions highlight the potential of AlSb as a material for optoelectronic coatings and light-reflective structures. Such behavior indicates efficient reflection of incident radiation at moderate photon energies while maintaining adequate transparency at higher energies, making AlSb suitable for multi-layer optical filters, solar concentrators, and infrared detector windows. The combination of a large refractive index and strong reflectivity confirms its promise for integration into photonic and energy-conversion devices, where precise control of light propagation and reflection is essential.

From the calculated static optical constants $n(0)$, $\epsilon(0)$, and $R(0)$, it can be observed that the hexagonal modification exhibits a slightly stronger optical response and higher dielectric polarizability than the cubic phase. These findings are consistent with the band gap values obtained using the mBJ functional and listed in Table 4. With increasing E_g , the values of ϵ , n , and R gradually decrease. This trend agrees with the general Penn model, which relates a larger band gap to lower dielectric polarizability. The consistency between the electronic and optical results confirms the reliability of the computational approach and the accuracy of the calculated data. The observed correlation between optical parameters and electronic structure highlights the intrinsic connection between chemical composition, density of states,

band gap width, and optical response of the material.

3.6. Thermoelectric properties

The Seebeck effect occurs when two different conductors or semiconductors are connected in series under a temperature gradient between their junctions [73–75]. This gradient drives the diffusion of electrons from the hot region toward the cold region, generating a thermoelectromotive force typically measured in microvolts per kelvin. The magnitude of this potential depends on the material type and the transport properties of charge carriers. The quality of a thermoelectric device is determined primarily by the Seebeck coefficient, where a larger coefficient indicates a higher efficiency in converting thermal energy into electricity.

In this study, the thermoelectric properties of AlSb were analyzed to understand how crystal structure and temperature influence the Seebeck coefficient (S), electrical conductivity (σ), electronic thermal conductivity (κ_e), and power factor (PF). These parameters were calculated using semiclassical Boltzmann transport theory as implemented in BoltzTraP:

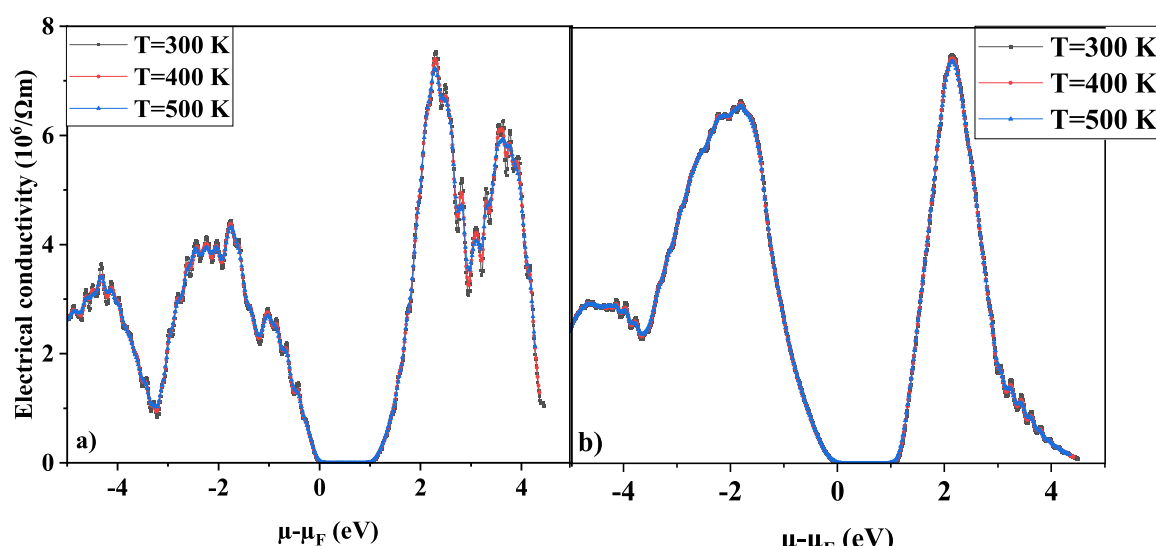


Fig. 17. Electrical conductivity of (a) cubic and (b) hexagonal AlSb phases at 300 K, 400 K, and 500 K.

$$S = \left(\frac{1}{eT} \right) \cdot \left(\frac{K_1}{K_0} \right),$$

$$\sigma = e^2 K_0,$$

$$k_e = \left(\frac{1}{T} \right) \cdot \left(\frac{K_2 - K_1^2}{K_0} \right),$$

$$PF = S^2 \sigma$$

where e is the elementary charge, T is the absolute temperature, and K_0 , K_1 , and K_2 are the transport integrals derived from the electronic band structure [61].

The Seebeck coefficient is highly sensitive to the electronic states near the Fermi level, and its magnitude and sign depend on the carrier type, effective mass, curvature of the band edges, and the position of the chemical potential. Evaluating S as a function of the Fermi level provides direct insight into intrinsic thermoelectric behavior and optimal doping conditions [76–79]. The dependence of S on chemical potential at 300, 400, and 500 K for both phases is shown in Figs. 15a and 15b. The interaction between electronic excitations and lattice vibrations observed in the optical spectra also plays a decisive role in the thermoelectric performance of AlSb. Materials with high dielectric constants and strong light-matter coupling often demonstrate enhanced carrier mobility and tunable electron-phonon scattering, improving both the Seebeck coefficient and electrical conductivity. Therefore, analysis of optoelectronic properties provides key insight into microscopic mechanisms governing charge and heat transport in both phases.

Both polymorphs exhibit strong thermopower, with the p-type cubic and hexagonal structures reaching approximately 1550 and 1545 $\mu\text{V/K}$ at 300 K, respectively. These values exceed the typical temperature-dependent Seebeck coefficients of bulk III-V semiconductors (300–600 $\mu\text{V/K}$) but are consistent with previous first-principles studies where S is computed as a function of the chemical potential rather than temperature [80–87], which often yields upper-limit theoretical values compared with classical temperature-dependent estimates [86,87]. In our calculations, the transport coefficients were obtained using the BoltzTraP2 code within the constant relaxation time approximation (CRTA), where the relaxation time τ is assumed to be independent of energy and temperature. This approximation, combined with the chemical-potential-based formulation of S , can enhance Seebeck magnitudes, particularly in materials with narrow carrier pockets or pronounced band-edge anisotropy. Therefore, the Seebeck coefficients exceeding 1500 $\mu\text{V/K}$ reported here should be regarded as intrinsic theoretical upper bounds rather than directly measurable experimental values. Nevertheless, the temperature-driven behavior of S and the favorable balance between thermopower and electrical conductivity

clearly confirm the intrinsic thermoelectric potential of both AlSb phases. Thus, the reported Seebeck coefficients above 1500 $\mu\text{V/K}$ should be viewed as intrinsic theoretical limits arising from the CRTA-based Boltzmann transport formulation rather than experimentally attainable values. As temperature rises, the coefficient increases due to enhanced carrier excitation, as shown in Figure S5. For the cubic phase, the Seebeck coefficient grows monotonically, while in the hexagonal phase it remains nearly zero between 150–250 K and begins to rise only above 250 K. This indicates that thermoelectric activity in the hexagonal structure emerges at higher temperatures compared to the cubic one.

In semiconductors, thermal conductivity is primarily governed by phonon transport, whereas in metals it is dominated by free electrons. For efficient thermoelectric materials, low thermal conductivity is essential to maintain a strong temperature gradient. Fig. 16 (a, b) shows the calculated thermal conductivity of both AlSb phases at 300 K, 400 K, and 500 K as a function of chemical potential. The reduction of thermal conductivity in both AlSb phases, especially above 600 K, is closely related to enhanced lattice anharmonicity and phonon-phonon scattering. At elevated temperatures, the increased vibrational amplitude of atoms strengthens three-phonon and higher-order scattering channels, which suppresses heat transport by shortening the phonon mean free path. This effect is more pronounced in the hexagonal $P6_3mc$ phase due to its lower lattice stiffness and higher anisotropy, which reduce the group velocity of acoustic phonons. As a result, κ decreases more strongly with temperature, enabling higher thermoelectric efficiency by increasing the $S^2\sigma/\kappa$ ratio. These observations are consistent with recent studies on anharmonic transport in AlSb and related III-V semiconductors.

Both phases exhibit nearly identical behavior. At room temperature, in the range 0.46–0.59 eV, the thermal conductivity for both structures is close to zero, corresponding to the optimal chemical potential range for maximizing thermoelectric efficiency. As the chemical potential moves away from this region, the thermal conductivity begins to increase, reducing the thermoelectric performance. To gain a deeper understanding of thermal transport, the temperature dependence of thermal conductivity was analyzed in the range from 150 to 1000 K, as shown in Figure S6. In the cubic phase, the thermal conductivity remains nearly zero up to about 400 K, after which it gradually increases. In the hexagonal phase, it stays close to zero up to approximately 600 K before showing a noticeable rise. At 300 K, the thermal conductivity of both phases is effectively zero, indicating very weak phonon-mediated heat transport at low temperatures.

When free electrons absorb heat, they gain kinetic energy and migrate toward the colder region of the material, generating an electric current. For a thermoelectric device to operate efficiently, the material must exhibit high electrical conductivity in order to minimize Joule heating losses. Figs. 17a, b presents the calculated electrical

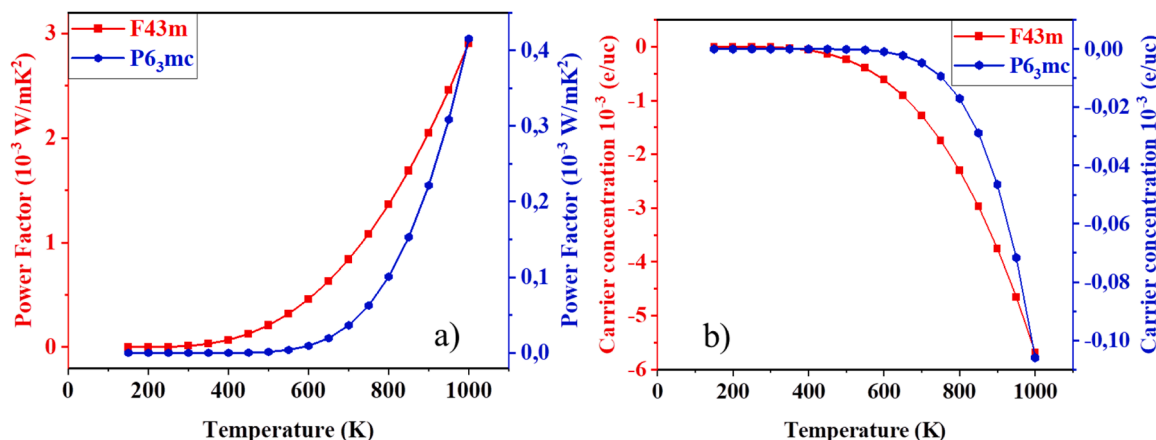


Fig. 18. (a) Temperature dependence of the power factor and (b) charge carrier concentration for the cubic (red) and hexagonal (blue) phases of AlSb.

conductivity of cubic and hexagonal AlSb phases at 300 K, 400 K, and 500 K. Both materials show similar temperature-dependent trends.

The plots reveal that the key chemical potential range for optimal conductivity in both p-type and n-type configurations lies between 0.46 and 0.59 eV. Beyond this range, electrical conductivity decreases, which defines the region where AlSb exhibits favorable thermoelectric performance. Within the specified window, both phases display a stable conductive behavior, confirming that AlSb maintains efficient charge transport properties across a broad range of chemical potentials.

The temperature dependence of electrical conductivity in the 150–1000 K range is shown in Figure S7. According to the results, the cubic phase of AlSb begins to exhibit noticeable conductivity at around 450 K, while the hexagonal modification becomes conductive near 650 K. As the temperature increases, the electrical conductivity of both phases grows exponentially due to thermal activation of charge carriers and a reduction in the band gap width. At 800 K, the electrical conductivity of the cubic phase reaches approximately 1.0×10^4 (S·m) $^{-1}$, whereas that of the hexagonal phase is about 7.5×10^3 (S·m) $^{-1}$, indicating higher carrier mobility and concentration in the cubic structure. The enhanced conductivity of the F-43 m phase correlates with its lower effective carrier mass and higher crystal symmetry, which facilitate more efficient charge transport.

The power factor (PF) reflects the ability of a material to convert thermal energy into electrical energy efficiently and depends on the balance between the Seebeck coefficient and electrical conductivity. As shown in Fig. 18a, both AlSb phases behave as typical semiconductors at low temperatures, where the concentration of thermally activated carriers is low and PF values are nearly zero. Starting at approximately 300 K for the cubic phase and 450 K for the hexagonal modification, a gradual increase in the power factor is observed, driven by carrier activation and improved electrical transport. At temperatures above 800 K, the hexagonal structure exhibits comparable or slightly higher PF values, which can be attributed to its lower thermal conductivity and enhanced phonon-electron scattering that suppresses carrier backflow. This temperature-dependent behavior confirms that AlSb is a promising candidate for high-temperature thermoelectric applications, where large thermal gradients are present. The observed trends are consistent with current research showing that for improving thermoelectric device efficiency above 600 K, it is essential to minimize thermal conductivity while maintaining a high $S^2\sigma / \kappa$ ratio.

Fig. 18b shows the temperature dependence of the charge carrier concentration. At low temperatures, the carrier density in both phases is close to zero, confirming the semiconducting nature of AlSb. As temperature increases, the carrier concentration rises steadily, following the expected thermal excitation trend typical for narrow-gap semiconductors, which further supports its potential use in high-efficiency thermoelectric converters and infrared energy-harvesting devices.

As temperature increases, the carrier concentration grows exponentially, particularly above 600 K, which is consistent with the mechanism of thermal generation of electron-hole pairs. The steeper increase observed for the cubic phase reflects its smaller band gap and higher density of states near the conduction band edge, resulting in stronger carrier excitation.

The combined analysis of Table S4, Figs. 15–18, and Figures S5–S7 demonstrates that the hexagonal P6₃mc phase of AlSb exhibits potentially higher thermoelectric efficiency at elevated temperatures. This improvement arises from the combination of high thermal stability, moderate electrical conductivity, and reduced lattice thermal conductivity, factors that are central to the optimization strategies of modern thermoelectric materials such as Bi₂Te₃, SnSe, and transition-metal oxynitrides. These results indicate that structural tuning and phonon engineering in AlSb-based systems can further enhance their high-temperature thermoelectric performance and broaden their applicability in energy conversion technologies. Finally, the correlation between crystal symmetry, phonon dispersion, and charge transport in AlSb becomes evident when comparing the two phases. The higher

symmetry of the cubic F-43 m structure results in more dispersive acoustic phonon branches and lower effective masses, which enhance carrier mobility and electrical conductivity. In contrast, the lower symmetry and anisotropic bonding environment of the hexagonal P6₃mc phase lead to flatter phonon modes, reduced group velocities, and stronger phonon scattering, which suppress thermal conductivity and improve thermoelectric efficiency at high temperatures. This interplay between structural symmetry, lattice dynamics, and electronic transport is a key factor governing the distinct thermoelectric responses of the cubic and hexagonal phases of AlSb.

4. Conclusion

A detailed theoretical analysis of AlSb in its cubic and hexagonal phases has been carried out to elucidate the interplay between structural, thermodynamic, electronic, optical, and thermoelectric characteristics that define its multifunctional potential. Both modifications were confirmed to be dynamically and mechanically stable, with the cubic phase exhibiting slightly higher thermodynamic stability, as supported by its lower formation energy and stronger interatomic bonding network. Phonon dispersion, elastic constants, and Debye temperature analyses indicate robust lattice integrity and favorable thermal behavior up to 1000 K. Electronic structure calculations revealed that both phases possess a direct band gap in the optimal range for infrared and solar-energy conversion technologies, while the pressure-dependent band-gap evolution underscores the possibility of band-structure engineering through strain or epitaxial control.

Optical modeling revealed strong absorption and high refractive indices comparable to established III-V semiconductors, suggesting AlSb's potential in infrared photodetectors, light-emitting diodes, and high-frequency optoelectronic devices. Thermoelectric simulations further showed that the hexagonal phase, owing to its reduced lattice stiffness and lower thermal conductivity, may outperform the cubic phase at elevated temperatures, highlighting AlSb as a viable candidate for energy-harvesting and waste-heat recovery systems.

Overall, this work bridges microscopic bonding characteristics and macroscopic functionalities, offering a comprehensive picture of AlSb as a dual-purpose semiconductor, combining optical transparency, electronic tunability, and thermoelectric efficiency. The insights presented herein provide a theoretical framework for future experimental efforts and guide the rational design of III-V-based materials for integrated optoelectronic and energy-conversion devices.

Funding

This work was supported by the Interstate Fund for Humanitarian Cooperation of the CIS Member States through the scientific project funded by the International Nanotechnology Innovation Center of the CIS (grant no. 25–113), and by the International Science and Technology Center (ISTC) (grant no. TJ-2726).

CRediT authorship contribution statement

Iskandar Raufov: Validation, Resources, Methodology, Investigation, Formal analysis, Data curation. **Dilshod Nematov:** Writing – review & editing, Writing – original draft, Supervision, Project administration, Investigation, Formal analysis. **Saidjafar Murozdoda:** Methodology, Data curation. **Sakhidod Sattorzoda:** Writing – original draft, Visualization, Software, Resources, Investigation, Formal analysis. **Anushervon Ashurov:** Writing – original draft, Funding acquisition, Conceptualization.

Declaration of competing interest

The authors declare that they have no known competing financial interests or personal relationships that could have appeared to influence

the work reported in this paper.

Supplementary materials

Supplementary material associated with this article can be found, in the online version, at [doi:10.1016/j.ctta.2025.100255](https://doi.org/10.1016/j.ctta.2025.100255).

Data availability

No data was used for the research described in the article.

References

- [1] M.A. Mohebpour, M.B. Tagani, First-principles study on the electronic and optical properties of AlSb monolayer, *Sci. Rep.* 13 (2023) 9925, <https://doi.org/10.1038/s41598-023-37081-5>.
- [2] W. Gouasmia, D. Boudjaadar, F. Oumelaz, O. Nemiri, R. Khenata, M. Sahnoun, A. Boudali, F. Rahmouni, A. Benhouria, M. Benhouria, First-principles assessment of the structural, phase transition, electronic, elastic and thermal properties of the semiconductor alloys Al_{1-x}Bi_x, *Eur. Phys. J. B* 98 (2025) 85, <https://doi.org/10.1140/epjb/s10051-025-00923-4>.
- [3] T. Feng, L. Lindsay, X. Ruan, Four-phonon scattering significantly reduces intrinsic thermal conductivity of solids, *Phys. Rev. B* 96 (2017), <https://doi.org/10.1103/PhysRevB.96.161201>, 161201(R).
- [4] X. Yang, T. Luo, X. Ruan, Stronger role of four-phonon scattering than three-phonon scattering in thermal conductivity of III-V semiconductors, *Phys. Rev. B* 100 (2019) 245203, <https://doi.org/10.1103/PhysRevB.100.245203>.
- [5] Z. Guo, Z. Han, D. Feng, G. Lin, X. Ruan, Sampling-accelerated prediction of phonon scattering rates for converged thermal conductivity and radiative properties, *NPJ. Comput. Mater.* 10 (2024) 31, <https://doi.org/10.1038/s41524-024-01215-8>.
- [6] Z. Guo, P. Roy Chowdhury, Z. Han, Y. Sun, D. Feng, G. Lin, X. Ruan, Fast and accurate machine-learning prediction of phonon scattering rates and lattice thermal conductivity, *NPJ. Comput. Mater.* 9 (2023) 95, <https://doi.org/10.1038/s41524-023-01020-9>.
- [7] Z. Huang, L. Wu, J. He, W. Li, J. Zhang, Y. Cai, The electrical, optical properties of AlSb polycrystalline thin films deposited by magnetron Co-sputtering without annealing, *Chin. Phys. B* 19 (2010) 127204, <https://doi.org/10.1088/1674-1056/19/12/127204>.
- [8] S. Baumann, G.E. Eperon, A. Virtuani, Q. Jeangros, D.B. Kern, D. Barrit, J. Schall, W. Nie, G. Oreski, M. Khenkin, C. Ulbrich, R. Peibst, J.S. Stein, M. Köntges, Stability and reliability of perovskite-containing solar cells and modules: degradation mechanisms and mitigation strategies, *Energy Environ. Sci.* 17 (2024) 7566–7601, <https://doi.org/10.1039/D4EE01898B>.
- [9] D. Zhang, F. Liu, S. Yang, et al., Degradation pathways in Perovskite solar cells and how to meet international standards, *Commun. Mater.* 3 (2022) 58, <https://doi.org/10.1038/s43246-022-00281-z>.
- [10] A.K.M.A. Shawon, S. Ur, I.-H. Kim, Synthesis and thermoelectric property elucidation of bulk AlSb prepared by powder metallurgy, *J. Electron. Mater.* 48 (2019) 7261–7270, <https://doi.org/10.1007/s11664-019-07726-1>.
- [11] M.A. Green, E.D. Dunlop, M. Yoshita, N. Kopidakis, K. Bothe, G. Siefer, D. Hinken, M. Rauer, J. Hohl-Ebinger, X. Hao, Solar cell efficiency tables (Version 64), *Prog. Photovolta.* 32 (2024) 425–441, <https://doi.org/10.1002/pip.3831>.
- [12] D. Zahn, Y. Grin, A.V. Ruban, Nucleation and growth in the NaCl→CsCl transition, *Phys. Rev. Lett.* 92 (2004) 250201, <https://doi.org/10.1103/PhysRevLett.92.250201>.
- [13] D. Varshney, R. Yogi, R.K. Singh, High-pressure B1-B2 transitions in III-V compounds: a first-principles study, *J. Phys. Chem. Solids.* 69 (2008) 2764–2772, <https://doi.org/10.1016/j.jpcs.2008.03.018>.
- [14] G. Sun, J. Wang, J. He, Y. Zhang, Z. Li, Four-phonon and normal scattering in 2D hexagonal crystals, *Int. J. Heat. Mass Transf.* 212 (2023) 124361, <https://doi.org/10.1016/j.ijheatmasstransfer.2023.124361>.
- [15] P. Staudinger, P. Caroff, K.A. Dick, A.R. Persson, S. Lehmann, et al., Exploring the size limitations of Wurtzite III-V film growth, *Nano Lett.* 19 (2019) 9151–9157, <https://doi.org/10.1021/acs.nanolett.9b04507>.
- [16] M. Hjort, S. Lehmann, J. Knutsson, D. Jacobsson, K.A. Dick, C. Thelander, Electronic and structural differences between wurtzite and Zinc-blende InAs nanowires, *ACS. Nano* 8 (2014) 12346–12355, <https://doi.org/10.1021/nn504795w>.
- [17] S. Mahmud, M.A. Ali, M.M. Hossain, M.M. Uddin, DFT-aided prediction of phase stability, optoelectronic and thermoelectric properties of A2AuScX6 (A = Cs, Rb; X = Cl, Br, I) double perovskites, *ArXiv.* (2023) arXiv:2310.00611, arxiv.org/abs/2310.00611.
- [18] S. Dahri, A. Jabar, L. Bahmad, L.B. Drissi, A. Laamara, R. The electronic, thermodynamic, thermoelectric and optical properties of Ca(InP)2_22: DFT study, *ArXiv.* (2023) arXiv:2312.01102, arxiv.org/abs/2312.01102.
- [19] H. Saadi, H. Kerrai, E.M. Jalal, M. El Bouziani, First-principles investigation of optical and thermoelectric properties of Na2InCu(F/Cl)6 double perovskites for energy harvesting devices, *Vacuum.* 236 (2025) 114149, <https://doi.org/10.1016/j.vacuum.2025.114149>.
- [20] H. Kerrai, N. Zaim, M. Kerouad, A. Zaim, Magnetic and electronic properties of double perovskite Sr2CrMoO6 for spintronic applications: insights from first-principles and Monte Carlo approaches, *Commun. Theor. Phys.* 76 (2024) 125701, <https://doi.org/10.1088/1572-9494/ad745e>.
- [21] H. Kerrai, N. Zaim, M. Kerouad, A. Zaim, Insight into electronic and magnetic properties of Ba2NiOsO6 double perovskite: a Monte Carlo study and a comparative investigation between TB-mBJ and GGA+U, *Comput. Mater. Sci.* 246 (2025) 113404, <https://doi.org/10.1016/j.commatsci.2024.113404>.
- [22] H. Kerrai, A. Zaim, M. Kerouad, First-principles study of the structural, magnetic and optoelectronic properties of double perovskite Ba2FeReO6, *Phys. Scr.* 99 (2024) 075983, <https://doi.org/10.1088/1402-4896/ad5883>.
- [23] H. Kerrai, A. Zaim, M. Kerouad, Tailoring the optoelectronic and transport properties of Cs2AgSb(Cl,Br)6 halide double perovskites for thermoelectric and optoelectronic applications, *Vacuum.* 225 (2024) 113267, <https://doi.org/10.1016/j.vacuum.2024.113267>.
- [24] S. Ur, A.K.M.A. Shawon, I.-H. Kim, Improvement of thermoelectric properties of AlSb by incorporation of Mg as *p*-type dopant, *Electron. Mater. Lett.* 16 (2020) 540–548, <https://doi.org/10.1007/s13391-020-00241-0>.
- [25] R.K. Singh, S. Singh, Structural phase transition and high-pressure elastic behavior of III-V semiconductors, *Phys. Rev. B* 39 (1) (1989) 671.
- [26] D. Nematov, Bandgap tuning and analysis of the electronic structure of the Cu2NiXS4 (X = Sn, Ge, Si) system: mBJ accuracy with DFT expense, *Chem. Inorganic Mater.* 1 (2023) 100001, <https://doi.org/10.1016/j.cinorg.2023.100001>.
- [27] M. Moin, A.W. Anwar, M.A. Ahmad, M. Yaseen, U. Ilays, S. Nabi, J. Hassan, First-principle calculations to investigate structural, electronic, mechanical, optical, and thermodynamic features of promising (La, In)-doped AlSb for optoelectronic applications, *J. Mol. Model.* 29 (7) (2023) 219.
- [28] S. Dong, Y. Li, Excitonic instability in 2D AlSb, *ArXiv.* (2021) arXiv:2102.07375, arxiv.org/abs/2102.07375.
- [29] J. Kim, S. Park, H. Choi, Mechanical properties of wurtzite and zinc-blende III-V compounds: *ab initio* study, *Comput. Mater. Sci.* 223 (2024) 111221, <https://doi.org/10.1016/j.commatsci.2023.112221>.
- [30] D. Nematov, I. Raufov, A. Ashurov, S. Sattorzoda, T. Najmaddinov, S. Nazriddinova, K. Yusupova, The promise of lead-free perovskites: can they replace toxic alternatives in solar cells and lead the future? *Int. J. Res. Innovat. Appl. Sci.* 10 (1) (2025) 353–377, <https://doi.org/10.51584/IJRAS.2025.100128>.
- [31] G. Kresse, J. Furthmüller, Efficient iterative schemes for ab initio total-energy calculations using a plane-wave basis set, *Phys. Rev. B* 54 (16) (1996) 11169, <https://doi.org/10.1103/PhysRevB.54.11169>.
- [32] P.E. Blöchl, Projector augmented-wave method, *Phys. Rev. B* 50 (24) (1994) 17953, <https://doi.org/10.1103/PhysRevB.50.17953>.
- [33] J. Sun, A. Ruzsinszky, J.P. Perdew, Strongly constrained and appropriately normed semilocal density functional, *Phys. Rev. Lett.* 115 (3) (2015) 036402, <https://doi.org/10.1103/PhysRevLett.115.036402>.
- [34] F. Tran, P. Blaha, Accurate band gaps of semiconductors and insulators with a semilocal exchange-correlation potential, *Phys. Rev. Lett.* 102 (22) (2009) 226401, <https://doi.org/10.1103/PhysRevLett.102.226401>.
- [35] J. Heyd, G.E. Scuseria, M. Ernzerhof, Hybrid functionals based on a screened coulomb potential, *J. Chem. Phys.* 118 (18) (2003) 8207–8215, <https://doi.org/10.1063/1.1564060>.
- [36] G.K.H. Madsen, J. Carrete, M.J. Verstraete, *BoltzTraP2*, a program for interpolating band structures and calculating semi-classical transport coefficients, *Comput. Phys. Commun.* 231 (2018) 140–145.
- [37] T.A. Nilsen, S.K. Patra, M. Breivik, B.O. Finland, Thermal dependence of the lattice constant and the Poisson ratio of AlSb above room temperature, *J. Cryst. Growth* 336 (1) (2011) 29–31, <https://doi.org/10.1016/j.jcrysgro.2011.09.037>.
- [38] K. Nakano, T. Sakai, Assessing the performance of the Tran-Blaha modified Becke-Johnson exchange potential for optical constants of semiconductors in the ultraviolet-visible light region, *J. Appl. Phys.* 123 (1) (2018), <https://doi.org/10.1063/1.5000357>.
- [39] K. Yang, B. Li, J. Zhang, W. Li, L. Wu, G. Zeng, W. Wang, C. Liu, L. Feng, Structural, optical and electrical properties of AlSb thin films deposited by pulsed laser deposition using aluminum-antimony alloying target, *Superlattices. Microstruct.* 102 (2017 Feb 1) 1–6, <https://doi.org/10.1016/j.spmi.2016.11.004>.
- [40] Becla P., Witt A.F. AlSb photonic detectors for gamma-ray spectroscopy. Progress report, October 1994–August 1995. Massachusetts Inst. of Technology (MIT), Cambridge, MA (United States); 1995 Dec 31.
- [41] P. Tang, B. Li, L. Feng, L. Wu, J. Zhang, W. Li, G. Zeng, W. Wang, C. Liu, Structural, electrical and optical properties of AlSb thin films deposited by pulsed laser deposition, *J. Alloys. Compd.* 692 (2017 Jan 25) 22–25, <https://doi.org/10.1016/j.jallcom.2016.08.321>.
- [42] P. Scherpelz, M. Govoni, I. Hamada, G. Galli, Implementation and validation of fully relativistic GW calculations: spin-Orbit coupling in molecules, nanocrystals, and solids, *J. Chem. Theory. Comput.* 12 (8) (2016) 3523–3544, <https://doi.org/10.1021/acs.jctc.6b00114>.
- [43] D. Nematov, Analysis of the optical properties and electronic structure of semiconductors of the Cu2NiXS4 (X = Si, Ge, Sn) family as new promising materials for optoelectronic devices, *J. Opt. Photon. Res.* 1 (2) (2024) 91–97, <https://doi.org/10.47852/bonviewJOPR42021819>.
- [44] D. Nematov, K. Kholmurodov, A DFT study of structure, electronic and optical properties of Se-doped kesterite Cu2ZnSnS4 (CZTSSe), *Letters Appl. NanoBioSci.* 3 (2023) 67, <https://doi.org/10.33263/LIANBLS123.067>.
- [45] D.D. Nematov, B.I. Makhsudov, K. Kholmurodov, Optimization optoelectronic properties $zn\cdot cd\cdot xe$ system for solar cell application: theoretical and experimental study, *Biointerface Res. Appl. Chem.* 13 (1) (2022) 90, <https://doi.org/10.33263/BRIAC131.090>.

[46] D. Nematov, Influence of iodine doping on the structural and electronic properties of CsSnBr_3 , *Int. J. Appl. Phys.* (2022) 7.

[47] D. Nematov, K. Kholmurodov, M. Husenzoda, A. Lyubchik, A. Burhonzoda, Molecular adsorption of H_2O on TiO_2 and TiO_2Y surfaces, *J. Hum. Earth Future* 3 (2) (2022) 213–222, <https://doi.org/10.28991/HEF-2022-03-02-07>.

[48] Z. Nizomov, M. Asozoda, D. Nematov, Characteristics of nanoparticles in aqueous solutions of acetates and sulfates of single and doubly charged cations, *Arab. J. Sci. Eng.* 48 (1) (2023) 867–873, <https://doi.org/10.1007/s13369-022-07128-2>.

[49] D. Nematov, K. Kholmurodov, D. Yuldasheva, K. Rakhamonov, I. Khojakhonov, Ab-initio study of structural and electronic properties of perovskite nanocrystals of the $\text{CsSn}[\text{Br}_1-\text{xIx}]_3$ family, *HighTech Innovat. J.* 3 (2) (2022) 140–150, <https://doi.org/10.28991/HIJ-2022-03-02-03>.

[50] N. Dilshod, K. Kholmizro, S. Aliona, F. Kahramon, G. Viktoriya, K. Tamerlan, On the optical properties of the $\text{Cu}_2\text{ZnSn}[\text{S}_{1-x}\text{Se}_x]$ 4 system in the IR range, *Trend. Sci.* 20 (2) (2023) 4058, <https://doi.org/10.48048/tis.2023.4058>.

[51] D. Nematov, Titanium dioxide and photocatalysis: a detailed overview of the synthesis, applications, challenges, advances and prospects for sustainable development, *J. Mod. Green Energy* 3 (6) (2024), <https://doi.org/10.53964/id.2025005>.

[52] D. Nematov, Molecular and dissociative adsorption of H_2O on ZrO_2/YSZ surfaces, *Int. J. Innovat. Sci. Modern Eng. (IJISME)* (2023), <https://doi.org/10.35940/ijisme.D7927.10111023>, 11, 10.

[53] D. Nematov, Investigation optical properties of the orthorhombic system $\text{CsSnBr}_3\text{-xIx}$: application for solar cells and optoelectronic devices, *J. Human. Earth. Future* 2 (4) (2021) 404–411, <https://doi.org/10.28991/HEF-2021-02-04-08>.

[54] D. Nematov, A. Burhonzoda, M. Khuseinov, K. Kholmurodov, A. Doroshkevych, N. Doroshkevych, M. Ibrahim, Molecular dynamics simulations of the DNA radiation damage and conformation behavior on a zirconium dioxide surface, *Egypt. J. Chem.* 62 (2019) 149–161, <https://doi.org/10.21608/ejchem.2019.12981.1811>.

[55] D.D. Nematov, A.S. Burhonzoda, K.T. Kholmurodov, A.I. Lyubchik, S.I. Lyubchik, A detailed comparative analysis of the structural stability and electron-phonon properties of ZrO_2 : mechanisms of water adsorption on t- ZrO_2 (101) and t- YSZ (101) surfaces, *Nanomaterials* 13 (19) (2023) 2657, <https://doi.org/10.3390/nano13192657>.

[56] B. Makhсудов, D. Nematov, M. Yarov, Combined X-ray diffraction analysis and quantum chemical interpretation of the effect of thermal neutrons on the geometry and electronic properties of CdTe , *J. Mod. Nanotechnol.* 4 (4) (2024) 2, <https://doi.org/10.53964/jmn.2024004>.

[57] D. Nematov, DFT calculations of the main optical constants of the $\text{Cu}_2\text{ZnSnSexS}_4\text{-x}$ system as high-efficiency potential candidates for solar cells, *Int. J. Appl. Power Eng.* 11 (4) (2022) 287–293, <https://doi.org/10.11591/ijape.v11.i4.pp287-293>.

[58] Z. Nizomov, S. Sodatdinov, R.K. Saidzoda, Influence of the height value of cylindrical specimens of copper grade M3 on the kinetics of their cooling and heat transfer processes, *Eng. Sci. Technol.* (2024) 316–325, <https://doi.org/10.37256/est.5220244118>.

[59] Z. Nizomov, S. Sodatdinov, R. Saidzoda, Analysis of thermal isotropy of parallelepiped shape of bronze samples for mechanical engineering applications, *J. Mod. Ind. Manuf.* 3 (9) (2024), <https://doi.org/10.53964/jmim.2024009>.

[60] R. El Mrabet, H. Kerrai, Insight into structural, electronic, and optical properties of binary CdX ($\text{X}=\text{S}$ and Te) chalcogenides, *Struct. Chem.* (2025), <https://doi.org/10.1007/s11224-025-02564-w>.

[61] H. Kerrai, A. Zaim, M. Kerouad, First-principles study of the structural, electronic, optical, and thermoelectric properties of tetragonal K_2PdX_4 ($\text{X}=\text{Cl}$, Br) compounds for energy harvesting, *Struct. Chem.* 36 (2025) 433–443, <https://doi.org/10.1007/s11224-024-02381-7>.

[62] S. Elhadfi, H. Kerrai, J. Chenouf, Z. Arbaoui, B. Fakrach, A. Rahmani, H. Chadli, Prediction of the structural, phonon, electronic, optical, and hydrogen storage properties of NaXH_3 ($\text{X}=\text{Ga}$, In) hydride perovskites, *Computat. Condensed Matter* 45 (2025) e01152, <https://doi.org/10.1016/j.cocom.2025.e01152>.

[63] M. Gajdóš, K. Hummer, G. Kresse, J. Furthmüller, Linear optical properties in the projector-augmented wave methodology, *Phys. Rev. B-Condensed Matter Mater. Phys.* (2006), <https://doi.org/10.1103/PhysRevB.73.045112>.

[64] J.M. Carcione, F. Cavallini, J. Ba, W. Cheng, A.N. Qadrour, On the kramers-kronig relations, *Rheol. Acta* (2019), <https://doi.org/10.1007/s00397-018-1119-3>.

[65] M.B. Shakir, G. Murtaza, A. Ayyaz, H. Khan, H. Irfan Ali, M. Touqir, Ab initio analysis of structural, optoelectronic, thermoelectric, and elastic characteristics of K_2MBiBr_6 ($\text{M}=\text{Na}$, Ag , and Cu) for green energy, *Opt. Quantum. Electron.* 56 (2024) 879, <https://doi.org/10.1007/s11082-024-06790-0>.

[66] M.B. Shakir, G. Murtaza, A. Ayyaz, H. Khan, M. Touqir, M. Naeem, R. Karmouch, H. Irfan Ali, A.A. Ibraheem, Probing the structural, electronic, thermodynamic, optical, and thermoelectric features of lead-free double perovskites $\text{Na}_2\text{ScAgZ}_6$ ($\text{Z}=\text{Br}$, I) for green energy harvesting, *Inorg. Chem. Commun.* 168 (2024) 112932, <https://doi.org/10.1016/j.inoche.2024.112932>.

[67] H. Khan, G. Murtaza, A. Ayyaz, M.B. Shakir, M. Touqir, K. Iqbal, A. Usman, S. Mumtaz, I.M. Moussa, Structural stability, optoelectronic, thermoelectric, and elastic characteristics of X_2ScBiO_6 ($\text{X}=\text{Mg}$, Ca , and Ba) double perovskites for energy harvesting: first-principles analysis, *Mater. Sci. Semicond. Process.* 185 (2025) 108911, <https://doi.org/10.1016/j.mssp.2024.108911>.

[68] H.U. Rehman, F. Abbas, M.U. Ashraf, I. Mamoon, K.A. Rao, A. Kaleem, S. Ali, A. A. Almunif, First-principles investigation of Bi- and Sb-doped ZnO : electronic, optical and mechanical insights, *Int. J. Modern Phys. C* (2025), <https://doi.org/10.1142/S0129183126500476>.

[69] H.U. Rehman, N. Muhammad, G. Murtaza, H.H. Raza, S.M. Ramay, M. Irfan, M. A. Rehman, The investigation of structural, electronic, thermal, and elastic properties of X_2ZnH_4 ($\text{X}=\text{K}$, Rb and Cs) for hydrogen storage applications: DFT study, *Opt. Quantum. Electron.* 56 (2024) 636, <https://doi.org/10.1007/s11082-024-06308-8>.

[70] H.U. Rehman, M. Jamil, N. Wang, G. Murtaza, M. Shafiq, M. Usman, Z. Usman, M. Zulfiqar, M.A. Khan, A DFT investigation on halide double perovskites X_2ScTlI_6 ($\text{X}=\text{Rb}$, Cs) for thermoelectric and optoelectronic applications, *Mater. Today Commun.* 40 (2024) 109806, <https://doi.org/10.1016/j.mtcomm.2024.109806>.

[71] H.U. Rehman, Z. Usman, M.U. Abdullah, A. Usman, Tuning the properties of SrI_2 : a DFT study on the contributions of S and Se doping, *Chem. Phys.* 598 (2025) 112841, <https://doi.org/10.1016/j.chemphys.2025.112841>.

[72] H.U. Rehman, N. Wang, E. Sun, M. Shoaib, Q. Zhu, A. Li, Y. Lu, Y. Sun, Stability and thermoelectric performance of binary chalcogenides: a first-principles perspective, *Solid. State Commun.* 405 (2025) 116139, <https://doi.org/10.1016/j.ssc.2025.116139>.

[73] G.J. Snyder, E.S. Toberer, Complex thermoelectric materials, *Nat. Mater.* 7 (2) (2008) 105–114, <https://doi.org/10.11591/ijape.v11.i4.pp287-293>.

[74] L.E. Bell, Cooling, heating, generating power, and recovering waste heat with thermoelectric systems, *Science* (1979) 321 (5895) (2008) 1457–1461, <https://doi.org/10.1126/science.1158899>.

[75] D. Nematov, M. Hojaberdi, Machine Learning-Driven Materials Discovery: Unlocking Next-Generation Functional Materials—A review, *Comput. Condens. Matter* 45 (2025) e01139, <https://doi.org/10.1016/j.cocom.2025.e01139>.

[76] M. Saeed, R. Khan, K.M. Abualnaja, A.M. Ali, K. Batool, G. Murtaza, Electronic profiles, optical absorption, and high thermoelectric performance of $\text{XCu}_3\text{GeSe}_4$ ($\text{X}=\text{K}$, Rb , Cs): a computational approach, *Int. J. Energy Res.* 2025 (1) (2025) 2992478, <https://doi.org/10.1155/er.2992478>.

[77] T. Yuan, G. Liu, G. Zhang, First-principles study on the influence of tensile deformation on the optoelectronic properties of the F-HfSe_2 system, *J. Mol. Model.* 31 (10) (2025) 319, <https://doi.org/10.1007/s00894-025-06504-7>.

[78] A. Marzegalli, F. Montalenti, E. Scalise, Polytypic quantum wells in Si and Ge: impact of 2D hexagonal inclusions on electronic band structure, *Nanoscale Horiz.* 9 (12) (2024) 2320–2325, <https://doi.org/10.1039/D4NH00355A>.

[79] Uglah, A.M., Saleem, K.B., Sultan, H.S., Maatki, C., Almeshaal, M.A., Selimedefidigil, F., & Kolsi, L. (2025). Numerical investigation on optimizing the couple geometry of a thermoelectric generator under various thermal conditions. Case studies in thermal engineering, 107191. <https://doi.org/10.1016/j.csite.2025.107191>.

[80] M.S. Dresselhaus, L.E. Bell, D.T. Morelli, When thermoelectrics reached the nanoscale, *Nat. Nanotechnol.* 8 (2013), <https://doi.org/10.1038/nnano.2013.129>.

[81] S. Tab, A. Boudali, M. Berber, H. Moujiri, Structural, elastic, electronic, and thermoelectric properties of chalcopyrite B_2BiN alloys: a first-principles study, *Appl. Phys. A* 126 (7) (2020), <https://doi.org/10.1007/s00339-020-03725-w>.

[82] A. Jayaraman, A.B. Kademan, M. Molli, DFT study on the carrier concentration and temperature-dependent thermoelectric properties of antimony selenide, *Indian J. Mater. Sci.* 2016 (2016), <https://doi.org/10.1155/2016/729647>.

[83] A. Ramanathan, J.M. Khalifeh, Enhanced thermoelectric properties of suspended mono- and bilayer of MoS_2 from first principles, *IEEE Trans. Nanotechnol.* 99 (2018), <https://doi.org/10.1109/TNANO.2018.2841640>, 1–1.

[84] A. Pandey, S.K. Pandey, Exploring the effect of strong electronic correlations in Seebeck Coefficient of the NdCoO_3 compound: using experimental and DFT+U approach, *Phys. Scr.* 99 (9) (2024), <https://doi.org/10.1088/1402-4896/ad6bf9>.

[85] Y. Benazouzi, H. Rozale, M.E.A.B. Hacene, D.D. Lucache, Electronic and thermoelectric properties in Li-based half-heusler compounds: a first principle study, *Annals West Univ. Timisoara - Phys.* 61 (1) (2020), <https://doi.org/10.2478/awutp-2019-0004>.

[86] G. Ding, G. Gao, K. Yao, High-efficient thermoelectric materials: the case of orthorhombic IV-VI compounds, *Sci. Rep.* 5 (1) (2015), <https://doi.org/10.1038/srep09567>.

[87] H. Yang, P. Boulet, M.-C. Record, Thermoelectric properties of Sb-S system compounds from DFT calculations, *Materials. (Basel)* 13 (21) (2020) 4707, <https://doi.org/10.3390/ma13214707>.